

# Torque equilibrium spin wave theory study of anisotropy and Dzyaloshinskii-Moriya interaction effects on the indirect $K$ -edge RIXS spectra of a triangular lattice antiferromagnet

Shangjian Jin,<sup>1</sup> Cheng Luo,<sup>1</sup> Trinanjan Datta,<sup>2,\*</sup> and Dao-Xin Yao<sup>1,†</sup>

<sup>1</sup>State Key Laboratory of Optoelectronic Materials and Technologies,  
School of Physics, Sun Yat-Sen University, Guangzhou 510275, China

<sup>2</sup>Department of Chemistry and Physics, Augusta University, 1120 15th Street, Augusta, Georgia 30912, USA  
(Dated: June 21, 2022)

We apply the recently formulated torque equilibrium spin wave theory (TESWT) to compute the  $1/S$ -order interacting  $K$ -edge bimagnon resonant inelastic x-ray scattering (RIXS) spectra of an anisotropic triangular lattice antiferromagnet with Dzyaloshinskii-Moriya (DM) interaction. We extend the interacting torque equilibrium formalism, incorporating the effects of DM interaction, to appropriately account for the zero-point quantum fluctuation that manifests as the emergence of spin Casimir effect in a noncollinear spin spiral state. Using inelastic neutron scattering data from  $\text{Cs}_2\text{CuCl}_4$  we fit the  $1/S$  corrected TESWT dispersion to extract exchange and DM interaction parameters. We use these new fit coefficients alongside other relevant model parameters to investigate, compare, and contrast the effects of spatial anisotropy and DM interaction on the RIXS spectra at various points across the magnetic Brillouin zone. We highlight the key features of the RIXS spectrum at the two inequivalent rotonlike points,  $M(0, 2\pi/\sqrt{3})$  and  $M'(\pi, \pi/\sqrt{3})$ , a behavior which is quite different from an isotropic triangular lattice system. While the roton RIXS spectra at the  $M$  point undergoes a spectral downshift with increasing anisotropy, the peak at the  $M'$  location loses its spectral strength without any shift. With the inclusion of DM interaction the spiral phase is more stable and the peak at both  $M$  and  $M'$  point exhibits a spectral upshift. Our calculation offers a practical example of how to calculate interacting RIXS spectra in a non-collinear quantum magnet using TESWT. Our findings provide an opportunity to experimentally test the predictions of interacting TESWT formalism using RIXS, a spectroscopic method currently in vogue.

**PACS number(s):** 78.70.Ck, 75.25.-J, 75.10.Jm

## I. INTRODUCTION

In a recent publication Cheng *et. al.*, Ref. 1, highlighted the features of the indirect  $K$ -edge resonant inelastic x-ray scattering (RIXS) bimagnon spectra of an isotropic triangular lattice antiferromagnet (TLAF). The TLAF is known to possess a  $120^\circ$  long range ordered state even after quantum fluctuations are considered [2–14]. The authors considered the self-energy corrections to the spin-wave spectrum to pinpoint the nontrivial effects of magnon damping and very weak spatial anisotropy on RIXS. It was shown that for a purely isotropic TLAF model, a multipeak RIXS spectrum appears which is primarily guided by the damping of magnon modes. Interestingly enough it was demonstrated that the roton momentum point is immune to magnon damping (for the isotropic case) with the appearance of a single-peak RIXS spectrum. It was suggested that this feature could be utilized as an experimental signature to search for or detect the presence of roton like excitations in the lattice. However, including XXZ anisotropy leads to additional peak splitting, including at the roton wave vector. Unfortunately, at present no theoretical guidance exists for experimentalists on how to interpret the RIXS spectra of the ordered phase in a geometrically frustrated triangular lattice quantum magnet, though a proposal has been put forward to detect spin-chirality terms in triangular-lattice Mott insulators via RIXS [15]. Furthermore, as discussed in this article the existing spin wave theory formulation used

for the isotropic case fails beyond the isotropic point and with Dzyaloshinskii-Moriya (DM) interaction included in the model.

Recently, the nature of the ground and excited states of the TLAF has garnered some attention [16–25]. A high magnetic field phase diagram study of the TLAF has also been performed [26]. An appropriate theoretical treatment of interactions must consider spin wave quantum fluctuation effects in a TLAF [27]. Zero-point quantum fluctuations of a non-collinear ordered quantum magnet gives rise to spin Casimir effect [28, 29]. As a spin analog of the Casimir effect in vacuum, the spin Casimir effect describes the various macroscopic Casimir forces and torques that can potentially emerge from the quantum spin system. The physical consequence of the casimir torque, generated due to the underlying lattice anisotropy, is the modification of the ordering wavevector, which is much smaller than the classical value. The modification in the ordering wavevector can cause the spin spiral state to become unstable, in turn rendering the standard spin wave theory expansion ( $1/S$ -SWT) approach inapplicable. Thus, the generic interacting spin wave theory is not appropriate. To remedy the effect of singular behavior (which are not precursors to the onset of quantum disordered phases) that naturally arises in noncollinear systems due to the presence of spin Casimir torque, Du *et. al.* [28, 29], proposed the torque equilibrium spin-wave theory (TESWT). The regularization scheme of TESWT formalism removes the naturally occurring divergences within the interacting  $1/S$ -SWT formalism of the anisotropic quantum lattice model. It was shown that TESWT gives a much closer final ordering vector to the results of series expansion (SE) and modified spin wave theory (MSWT) method [18, 30]. Furthermore, its prediction of

\* Corresponding author: [tdatta@augusta.edu](mailto:tdatta@augusta.edu)

† Corresponding author: [yaodaoo@mail.sysu.edu.cn](mailto:yaodaoo@mail.sysu.edu.cn)

the phase diagram is consistent with the previous numerical studies [18, 30].

Historically, the concept of a roton minimum and a rotonlike point in the TLAF was introduced by Zheng *et. al.* [31, 32]. Using SE method the authors identified a local minimum in the magnon dispersion at the high symmetry  $M'$  point,  $(\pi, \pi/\sqrt{3})$ . Drawing analogy with the appearance of a similar dip (local minimum) that is observed in the excitation spectra of superfluid  $^4\text{He}$ [33] and the fractional quantum Hall effect [34], the authors proposed the “roton” nomenclature to describe the minimum in the magnon dispersion. The dip in the spectrum is also present at the other high symmetry  $M$  point,  $(0, 2\pi/\sqrt{3})$ , in the middle of the magnetic Brillouin zone (MBZ) face edge. Zheng *et. al.* noted that a roton minimum is absent in the linear spin wave theory (LSWT) spectrum. Thus, the occurrence of the rotonlike point is a consequence of quantum fluctuations arising in a frustrated magnetic material. In a subsequent publication the concept of the rotonlike point was extended to the case of an anisotropic lattice by Fjaerestad *et.al.* [27].

Further support of the roton feature was provided by the  $1/S$ -SWT study of Starykh *et.al.* [35]. Based on their work it was proposed that rotons are part of a global renormalization (weak local minimum), with large regions of (almost) flat dispersion. The appearance of rotonlike minima and what was dubbed as a roton excitation has also been studied in an anisotropic spin-1/2 TLAF from the perspective of an algebraic vortex liquid theory [36, 37]. Several anomalous roton minima were predicted in the excitation spectrum in the regime of lattice anisotropy where the canted Neel state appears. From the perspective of the algebraic vortex liquid theory formulated in terms of fermionic vortices in a dual field theory, it was proposed that the roton is a vortex anti-vortex excitation, thereby, lending credence to use of the word roton as an apt description. Rotons have also been predicted to exist in field induced TLAF magnetic systems [38]. The field-induced transformations in the dynamical response of the XXZ model create the appearance of rotonlike minima at the  $K$  point. Additionally, a square lattice system with  $J'/J > 2$  has been predicted to support the roton minima [31]. Experimental evidence of the rotonlike point can be found in recent inelastic neutron scattering (INS) spectrum of the  $\alpha\text{-CaCr}_2\text{O}_2$  system [10, 11]. Examples of TLAF where anisotropy and DM interaction are present are plethora [6–12, 27, 39–41]. In this article, we utilize material parameters relevant to  $\text{Cs}_2\text{CuCl}_4$  to elucidate the  $K$ -edge RIXS behavior of the rotonlike points.

With advancements in instrumental resolution of the next-generation synchrotron radiation sources, RIXS spectroscopy presents itself as a novel experimental tool to investigate the nature of the bimagnon RIXS spectra and the influence of the roton. As a spectroscopic technique RIXS has the ability to probe both single-magnon and multimagnon excitations across the entire MBZ. Using RIXS it is possible to probe high energy excitations in cuprates [42]. Considering the physical behavior that has been studied within the context of RIXS TLAF and the fact that departures from the isotropic triangular lattice geometry is a norm in a frustrated TLAF, this begs

the question – “What is the influence of spatial anisotropy and also DM interaction on the  $K$ -edge indirect RIXS bimagnon spectra at the rotonlike points and the other MBZ points of an anisotropic triangular lattice?”

In this article we apply TESWT to our quantum Heisenberg model with spatial anisotropy and DM interaction on a triangular lattice. Using a TESWT upto first order in  $1/S$ , we compute the final ordering vector, the spin-wave energy and phase diagram with different anisotropy parameters. We find the phase diagram has a consistent behavior with vector  $\mathbf{Q}$ . We find that the presence of a relatively small DM interaction can make the spiral state more stable. We calculate the interplay of X-ray scattering and bimagnon excitation. We find that the evolution of the RIXS spectra at rotonlike point is non-trivial. In the isotropic case all the rotonlike points are identical due to the  $60^\circ$  rotation symmetry of the underlying isotropic triangular lattice. However, in the presence of symmetry breaking anisotropy and DM interaction terms the equivalence breaks down to give rise to two distinct points –  $M$  and  $M'$ , see Fig. 9. Thus we investigate and track the evolution of the spectra at these two points separately. With increasing anisotropy the spectral weight at these points vanish, even though the rotonlike points lie outside the region of magnon damping. Additionally, we find that the RIXS spectra at the rotonlike  $M$  point undergoes a spectral downshift and near complete suppression. However, the peak at the  $M'$  point the location of the peak is stable, albeit suppressed as the strength of the perturbations are increased. We also track the bimagnon RIXS evolution at the  $Y$  point in the Brillouin zone to compare and contrast with the behavior at the rotonlike points. The spectrum at  $Y$  shows more peaks than at  $M$  or  $M'$ . Thus, the roton excitation spectrum is more stable.

This paper is organized as follows. In Sec. II we introduce the model spin-1/2 anisotropic TLAF with DM interaction. In Sec. III A we state the spin wave formalism required to compute the wave vector renormalization (Sec. III B) and renormalized dispersion (Sec. III C). In Sec. IV, we extend the applicability of the TESWT formalism to include the effects of DM interaction. In Sec. IV A, we elaborate on the TESWT method, compute the ordering vector and dispersion, and perform a TESWT INS fitting (Sec. IV B). We then calculate the phase diagram in Sec. IV C. In Sec. V we compute the indirect RIXS spectra. In Sec. V A we compute the non-interacting bi- and trimagnon spectrum. In Sec. V B we outline the formalism to compute the RIXS spectrum. In Sec. V C we compute the interacting bimagnon RIXS spectrum by including the quartic interactions at points along the MBZ. We also track the evolution of the roton energy to provide a physical explanation of the trend exhibited by the RIXS spectra with anisotropy and DM interaction. In Sec. V D we state the results for the total indirect  $K$ -edge RIXS intensity. Finally, in Sec. VI we provide our conclusions.

## II. MODEL HAMILTONIAN

The antiferromagnetic Heisenberg model on the anisotropic triangular lattice has recently attracted many interests [43],

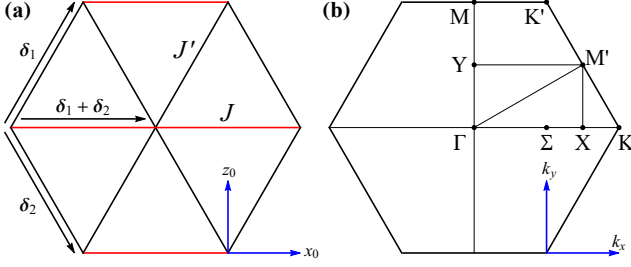


FIG. 1. Sketch of the triangular lattice and the MBZ. (a) The anisotropic triangular lattice with exchange constant  $J$  along the horizontal bonds and  $J'$  along the diagonal (zigzag) bonds. The lattice vectors are denoted by  $\delta_{1,2}$ . (b) The first Brillouin zone and the high-symmetry points, defined as  $\Gamma = (0,0)$ ,  $\Sigma = (2\pi/3,0)$ ,  $X = (\pi,0)$ ,  $K = (4\pi/3,0)$ ,  $K' = (2\pi/3,2\pi/\sqrt{3})$ ,  $M' = (\pi,\pi/\sqrt{3})$ ,  $M = (0,2\pi/\sqrt{3})$  and  $Y = (0,\pi/\sqrt{3})$ .

and is widely believed to well describe the compounds  $\text{Cs}_2\text{CuBr}_4$  and  $\text{Cs}_2\text{CuCl}_4$ . While  $\text{Cs}_2\text{CuCl}_4$  exhibits spin-liquid behavior over a broad temperature range [41, 44], the  $\text{Cs}_2\text{CuBr}_4$  compound shows a magnetic ordered ground state with spiral order in zero magnetic field [6]. For  $\alpha\text{-CaCr}_2\text{O}_4$ , though it is reported to have two inequivalent  $\text{Cr}^{3+}$  ions and four different exchange interactions, the nature of the distortion is such that the average of the exchange interactions along any direction is approximately equal.

We consider the spin-1/2 antiferromagnetic Heisenberg model on the anisotropic triangular lattice, weakly perturbed by an additional Dzyaloshinskii-Moriya (DM) interaction, as described by

$$\mathcal{H} = \sum_{\langle ij \rangle} J_{ij} \mathbf{S}_i \cdot \mathbf{S}_j + H_{\text{DM}}, \quad (1)$$

where  $\langle ij \rangle$  refers to nearest-neighbor bonds on the triangular lattice,  $J_{ij} = J$  denotes the exchange constants along the horizontal bonds and  $J_{ij} = J'$  the diagonal bonds, see Fig. 1. The asymmetric DM interaction between neighboring spins is given by

$$H_{\text{DM}} = - \sum_i \mathbf{D} \cdot [\mathbf{S}_i \times (\mathbf{S}_{i+\delta_1} + \mathbf{S}_{i+\delta_2})], \quad (2)$$

where  $\mathbf{D} = (0, D, 0)$  with  $(D > 0)$  and  $\delta_{1,2}$  are nearest neighboring vectors along diagonal bonds shown in Fig. 1. In the classical limit, the spin operators are replaced by three-component vectors

$$\mathbf{S}_i/S = \cos(\mathbf{Q} \cdot \mathbf{r}_i) \hat{z}_0 + \sin(\mathbf{Q} \cdot \mathbf{r}_i) \hat{x}_0, \quad (3)$$

where the spin forms a spiral with the ordering vector  $\mathbf{Q}$ . The classical ground state energy is given by

$$E_0(\mathbf{Q}) = 3NJS^2(\lambda_{\mathbf{Q}} - \eta_{\mathbf{Q}}) = 3NJS^2\gamma_{\mathbf{Q}}, \quad (4)$$

with

$$\lambda_{\mathbf{k}} = \frac{1}{3}(\cos k_x + 2\alpha \cos \frac{k_x}{2} \cos \frac{\sqrt{3}}{2} k_y), \quad (5)$$

$$\eta_{\mathbf{k}} = \frac{2}{3}\eta \sin \frac{k_x}{2} \cos \frac{\sqrt{3}}{2} k_y, \quad (6)$$

where the dimensionless ratios  $\alpha = J'/J$  and  $\eta = D/J$  denote the relative interaction strengths. For the determination of the ordering vector  $\mathbf{Q}$ , we have to minimize the classical ground state energy

$$\nabla_{\mathbf{Q}} E_0(\mathbf{Q}) = 0, \quad (7)$$

which amounts to finding the roots of the equations

$$\begin{cases} \sin Q_x + \alpha \sin \frac{Q_x}{2} \cos \frac{\sqrt{3}}{2} Q_y + \eta \cos \frac{Q_x}{2} \cos \frac{\sqrt{3}}{2} Q_y = 0, \\ \alpha \cos \frac{Q_x}{2} \sin \frac{\sqrt{3}}{2} Q_y - \eta \sin \frac{Q_x}{2} \sin \frac{\sqrt{3}}{2} Q_y = 0. \end{cases} \quad (8)$$

Anticipating that this condition leads to a spiral along the  $x$  axis  $\mathbf{Q} = (Q_0, 0)$ , we obtain the solution in the absence of DM interaction

$$Q_0 = \begin{cases} 2 \arccos(-\frac{\alpha}{2}), & \alpha < 2, \\ 2\pi, & \alpha \geq 2. \end{cases} \quad (9)$$

It is not clear whether the classical ordering vector correctly describes the long-ranger order in the quantum frustrated system. In fact, the classical wave vector will be renormalized by quantum fluctuations as will be discussed in Sec. IV A.

### III. LINEAR SPIN-WAVE THEORY

#### A. $1/S$ expansion

Before we set up the spin-wave expansion, it is convenient to transform the spin components in the laboratory frame  $(x_0, z_0)$  to the rotating frame  $(x, z)$  through

$$S_i^{x_0} = S_i^z \sin \theta_i + S_i^x \cos \theta_i, \quad (10)$$

$$S_i^{z_0} = S_i^z \cos \theta_i - S_i^x \sin \theta_i, \quad (11)$$

where  $\theta_i = \mathbf{Q} \cdot \mathbf{r}_i$ . The rotating Hamiltonian takes the form

$$\begin{aligned} \mathcal{H} = \sum_{\langle ij \rangle} & J_{ij} S_i^y S_j^y + J_{ij}^+ (S_i^z S_j^z + S_i^x S_j^x) \\ & + J_{ij}^- (S_i^z S_j^x - S_i^x S_j^z), \end{aligned} \quad (12)$$

and we have defined

$$J_{ij}^+ = J_{ij} \cos(\theta_i - \theta_j) + D_{ij} \sin(\theta_i - \theta_j), \quad (13)$$

$$J_{ij}^- = J_{ij} \sin(\theta_i - \theta_j) - D_{ij} \cos(\theta_i - \theta_j). \quad (14)$$

SWT amounts to applying the Holstein-Primakoff (HP) transformation to bosonize the rotating Hamiltonian (12)

$$S_i^z = S - n_i, \quad S_i^- = a^\dagger \sqrt{2S - n_i}, \quad S_i^+ = (S_i^-)^\dagger, \quad (15)$$

where  $n_i = a_i^\dagger a_i$ . Under the assumption of diluteness of the HP boson gas,  $n_i/(2S) < 1$ , one arrives at the interacting spin-wave Hamiltonian to the first order expansion of the square root

$$\mathcal{H} = E_0(\mathbf{Q}) + H_2 + H_3 + H_4, \quad (16)$$

where the first term is the classical energy and  $H_n$  denote terms of the  $n$  power in the HP boson operators  $a^\dagger(a)$ .

### B. Quadratic terms: first-order corrected LSWT

After Fourier transformation we obtain the quadratic Hamiltonian in momentum space,

$$H_2 = \sum_{\mathbf{k}} \left[ A_{\mathbf{k}} a_{\mathbf{k}}^\dagger a_{\mathbf{k}} + \frac{B_{\mathbf{k}}}{2} (a_{\mathbf{k}}^\dagger a_{-\mathbf{k}}^\dagger + a_{-\mathbf{k}} a_{\mathbf{k}}) \right], \quad (17)$$

with

$$\begin{aligned} A_{\mathbf{k}} &= 3JS [\lambda_{\mathbf{k}} + \xi_{\mathbf{k}} - 2\gamma_{\mathbf{Q}}], \\ B_{\mathbf{k}} &= 3JS [\xi_{\mathbf{k}} - \lambda_{\mathbf{k}}], \end{aligned} \quad (18)$$

where

$$\xi_{\mathbf{k}} = \frac{1}{2} (\gamma_{\mathbf{Q}+\mathbf{k}} + \gamma_{\mathbf{Q}-\mathbf{k}}). \quad (19)$$

Diagonalization of  $H_2$  is performed with the canonical Bogoliubov transformation

$$a_{\mathbf{k}} = u_{\mathbf{k}} b_{\mathbf{k}} + v_{\mathbf{k}} b_{-\mathbf{k}}^\dagger, \quad (20)$$

with the parameters  $u_{\mathbf{k}}$  and  $v_{\mathbf{k}}$  defined as

$$u_{\mathbf{k}} = \sqrt{\frac{A_{\mathbf{k}} + \varepsilon_{\mathbf{k}}}{2\varepsilon_{\mathbf{k}}}}, \quad v_{\mathbf{k}} = -\frac{B_{\mathbf{k}}}{|B_{\mathbf{k}}|} \sqrt{\frac{A_{\mathbf{k}} - \varepsilon_{\mathbf{k}}}{2\varepsilon_{\mathbf{k}}}}. \quad (21)$$

As a result we obtain the linear spin-wave dispersion

$$\varepsilon_{\mathbf{k}} = \sqrt{A_{\mathbf{k}}^2 - B_{\mathbf{k}}^2}. \quad (22)$$

It is noted that the magnon spectrum has zeros at  $\mathbf{k} = 0$  while a gap is opened at  $\mathbf{k} = \mathbf{Q}$  in the presence of DM interaction. The diagonalized Hamiltonian  $H_2$  is given by

$$H_2 = E_2(\mathbf{Q}) + \sum_{\mathbf{k}} \varepsilon_{\mathbf{k}} b_{\mathbf{k}}^\dagger b_{\mathbf{k}}, \quad (23)$$

where the zero-point energy

$$E_2(\mathbf{Q}) = 3NSJ\gamma_{\mathbf{Q}} + \frac{1}{2} \sum_{\mathbf{k}} \varepsilon_{\mathbf{k}}, \quad (24)$$

is the 1/S correction to the classical ground-state energy. Generally, the first-order correction of LSWT  $\mathbf{Q}_1 = \mathbf{Q}_0 + \Delta\mathbf{Q}$  is determined by minimizing the sum  $E_0(\mathbf{Q}) + E_2(\mathbf{Q})$

$$\nabla_{\mathbf{Q}}[E_0(\mathbf{Q}) + E_2(\mathbf{Q})] = 0. \quad (25)$$

Neglecting higher order terms, we obtain

$$\nabla_{\mathbf{Q}}[E_0(\mathbf{Q}_1) + E_2(\mathbf{Q}_1)] = \nabla_{\mathbf{Q}}E_2(\mathbf{Q}_0) + \Delta\mathbf{Q} \cdot \mathbf{K} = 0, \quad (26)$$

with

$$K_{\alpha\beta} = \frac{\partial^2 E_0(\mathbf{Q}_0)}{\partial Q_\beta \partial Q_\alpha}. \quad (27)$$

A straightforward calculation gives 1/S correction to the classical wave vector

$$\Delta\mathbf{Q} = -\mathbf{w} \cdot \mathbf{K}^{-1}, \quad (28)$$

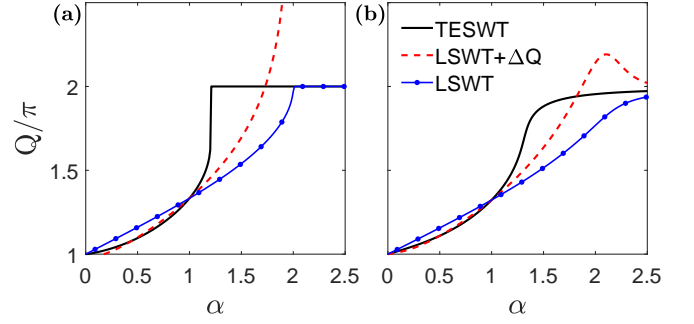


FIG. 2. The evolution of ordering wave vector  $Q$  for the  $S = \frac{1}{2}$  spiral antiferromagnet on the anisotropic triangular lattice as a function of  $\alpha = J'/J$ . The ordering vectors of TESWT, LSWT and 1/S corrected LSWT are compared. (a)  $\eta = D/J = 0$ , (b)  $\eta = D/J = 0.05$ .

where

$$w_\alpha = \frac{\partial E_2(\mathbf{Q}_0)}{\partial Q_\alpha}. \quad (29)$$

In Fig. 2 we display the variation of the ordering wave vector renormalization against lattice anisotropy computed using LSWT, 1/S corrected LSWT, and TESWT. It is clear that while the LSWT formulation extends the spiral phase region, the first-order correction from 1/S-LSWT gives an unphysical result as  $\alpha \rightarrow 2$  while  $\eta = 0$ . Inclusion of DM interaction rounds the singularity with an angle that is greater than  $2\pi$ . The root cause of this divergence originates from spin Casimir torque [28, 29]. In a frustrated spiral system, the strong quantum fluctuation effect leads to failure in the first-order correction. In Sec. IV we will discuss and implement the TESWT approach which offers a solution to this issue. The equations to generate the TESWT results are reported in that section.

### C. Cubic and quartic terms: renormalized dispersion

The 1/S correction to the spin wave dispersion has to be accounted for in a non-collinear structure. The interplay of magnon decay as it arises from the non-collinear structure is also considered [45–47]. The three-boson term that arises from the coupling between transverse and longitudinal fluctuations in the noncollinear spin structure takes the form [48],

$$H_3 = -\sqrt{\frac{S}{2}} \sum_{\langle ij \rangle} J_{ij}^- [a_i^\dagger a_i (a_j^\dagger + a_j) - a_j^\dagger a_j (a_i^\dagger + a_i)], \quad (30)$$

In momentum space, we obtain

$$H_3 = \frac{3JSi}{2} \sqrt{\frac{3}{2SN}} \sum_{1+2=3} (\tilde{\gamma}_1 + \tilde{\gamma}_2) (a_1^\dagger a_2^\dagger a_3 - a_3^\dagger a_1 a_2), \quad (31)$$

where we have defined

$$\tilde{\gamma}_{\mathbf{k}} = \frac{1}{\sqrt{3}} (\gamma_{\mathbf{Q}+\mathbf{k}} - \gamma_{\mathbf{Q}-\mathbf{k}}). \quad (32)$$

Performing the Bogoliubov transformation in  $H_3$  we obtain the interaction terms expressed via the magnon operators

$$H_3 = \frac{1}{2!} \sum_{1+2=3} V_a(1, 2; 3)(b_1^\dagger b_2^\dagger b_3 + \text{H.c.}) + \frac{1}{3!} \sum_{1+2+3=0} V_b(1, 2, 3)(b_1^\dagger b_2^\dagger b_3^\dagger + \text{H.c.}), \quad (33)$$

where we have adopted the convention that  $1 = \mathbf{k}_1$ ,  $2 = \mathbf{k}_2$ , etc. The three-boson decay and source vertices are respectively given by

$$V_{a,b}(1, 2; 3) = 3Ji\sqrt{\frac{3S}{2N}}\bar{V}_{a,b}(1, 2; 3), \quad (34)$$

with  $\bar{V}_{a,b}$  given by

$$\bar{V}_a(1, 2; 3) = \bar{\gamma}_1(u_1 + v_1)(u_2 u_3 + v_2 v_3) + \bar{\gamma}_2(u_2 + v_2)(u_1 u_3 + v_1 v_3) - \bar{\gamma}_3(u_3 + v_3)(u_1 v_2 + v_1 u_2), \quad (35)$$

$$\bar{V}_b(1, 2, 3) = \bar{\gamma}_1(u_1 + v_1)(u_2 v_3 + v_2 u_3) + \bar{\gamma}_2(u_2 + v_2)(u_1 v_3 + v_1 u_3) + \bar{\gamma}_3(u_3 + v_3)(u_1 v_2 + v_1 u_2). \quad (36)$$

We notice that the three-magnon vertices are of order  $1/\sqrt{S}$  relative to the linear spin-wave Hamiltonian and they must occur in pairs in any self-energy or polarization diagram. The quartic term  $H_4$  in the interacting spin-wave Hamiltonian (16) reads

$$H_4 = \sum_{\langle ij \rangle} \left[ \frac{1}{2} J_{ij}^+ a_i^\dagger a_j^\dagger a_i a_j + \frac{1}{8} (J_{ij} - J_{ij}^+)(a_i^\dagger a_i a_j a_j + a_j^\dagger a_j a_i a_i) - \frac{1}{8} (J_{ij} + J_{ij}^+)(a_j^\dagger a_i^\dagger a_i a_i + a_j^\dagger a_j^\dagger a_j a_j) \right] + \text{H.c.} \quad (37)$$

To obtain the explicit forms of the quasiparticle representation of  $H_4$ , we introduce the following mean-field averages:

$$n_{\mathbf{k}} = \langle a_{\mathbf{k}}^\dagger a_{\mathbf{k}} \rangle = \frac{A_{\mathbf{k}} - \varepsilon_{\mathbf{k}}}{2\varepsilon_{\mathbf{k}}}, \Delta_{\mathbf{k}} = \langle a_{\mathbf{k}} a_{-\mathbf{k}} \rangle = -\frac{B_{\mathbf{k}}}{2\varepsilon_{\mathbf{k}}}. \quad (38)$$

The Hartree-Fock decoupling of the  $H_4$  yields the quadratic Hamiltonian

$$\delta H_2 = \sum_{\mathbf{k}} \left[ \delta A_{\mathbf{k}} a_{\mathbf{k}}^\dagger a_{\mathbf{k}} + \frac{1}{2} \delta B_{\mathbf{k}} (a_{\mathbf{k}}^\dagger a_{-\mathbf{k}}^\dagger + a_{-\mathbf{k}} a_{\mathbf{k}}) \right], \quad (39)$$

where

$$\delta A_{\mathbf{k}} = A_{\mathbf{k}} + \frac{1}{2SN} \sum_{\mathbf{q}} \frac{1}{\varepsilon_{\mathbf{q}}} \left[ A_{\mathbf{q}} (A_{\mathbf{k}-\mathbf{q}} + B_{\mathbf{k}-\mathbf{q}} - A_{\mathbf{k}} - A_{\mathbf{q}}) + B_{\mathbf{q}} \left( \frac{B_{\mathbf{k}}}{2} + B_{\mathbf{q}} \right) \right], \quad (40)$$

$$\delta B_{\mathbf{k}} = B_{\mathbf{k}} - \frac{1}{2SN} \sum_{\mathbf{q}} \frac{1}{\varepsilon_{\mathbf{q}}} \left[ B_{\mathbf{q}} (A_{\mathbf{k}-\mathbf{q}} + B_{\mathbf{k}-\mathbf{q}} - \frac{A_{\mathbf{k}}}{2} - \frac{A_{\mathbf{q}}}{2}) + A_{\mathbf{q}} \left( B_{\mathbf{k}} + \frac{B_{\mathbf{q}}}{2} \right) \right], \quad (41)$$

We then obtain the Hartree-Fock corrected  $H_4$

$$\delta H_2 = \sum_{\mathbf{k}} \left[ \delta \varepsilon_{\mathbf{k}} b_{\mathbf{k}}^\dagger b_{\mathbf{k}} + \frac{O_{\mathbf{k}}}{2} (b_{\mathbf{k}}^\dagger b_{-\mathbf{k}}^\dagger + b_{\mathbf{k}} b_{-\mathbf{k}}) \right], \quad (42)$$

where

$$\delta \varepsilon_{\mathbf{k}} = (u_{\mathbf{k}}^2 + v_{\mathbf{k}}^2) \delta A_{\mathbf{k}} + 2u_{\mathbf{k}} v_{\mathbf{k}} \delta B_{\mathbf{k}}, \quad (43)$$

$$O_{\mathbf{k}} = (u_{\mathbf{k}}^2 - v_{\mathbf{k}}^2) \delta B_{\mathbf{k}} + 2u_{\mathbf{k}} v_{\mathbf{k}} \delta A_{\mathbf{k}}. \quad (44)$$

Finally, the normal-ordered quartic term  $\tilde{H}_4$  in the quasiparticle representation describes the multi-magnon interactions. In the hierarchy of  $1/S$  expansion, terms relevant for our calculations are the lowest order irreducible two-magnon scattering amplitude

$$\tilde{H}_4^{2-p} = \sum_{\mathbf{k}_1 + \mathbf{k}_2 = \mathbf{k}_3 + \mathbf{k}_4} V_c(\mathbf{k}_1, \mathbf{k}_2; \mathbf{k}_3, \mathbf{k}_4) b_{\mathbf{k}_1}^\dagger b_{\mathbf{k}_2}^\dagger b_{\mathbf{k}_3} b_{\mathbf{k}_4}, \quad (45)$$

with the vertex function given by

$$V_c(1, 2; 3, 4) = \frac{1}{8SN} \left\{ - (B_1 + B_2 + B_4)(u_1 u_2 u_3 v_4 + v_1 v_2 v_3 u_4) - (B_1 + B_2 + B_3)(u_1 u_2 v_3 u_4 + v_1 u_2 u_3 v_4) - (B_2 + B_3 + B_4)(u_1 v_2 u_3 u_4 + v_1 u_2 v_3 v_4) - (B_1 + B_3 + B_4)(u_1 v_2 v_3 v_4 + v_1 u_2 u_3 u_4) + [(C_{1-3} + C_{2-3} + C_{1-4} + C_{2-4}) - (A_1 + A_2 + A_3 + A_4)](u_1 u_2 u_3 u_4 + v_1 v_2 v_3 v_4) + [(C_{1+2} + C_{3+4} + C_{1-3} + C_{2-4}) - (A_1 + A_2 + A_3 + A_4)](u_1 v_2 u_3 v_4 + v_1 u_2 v_3 u_4) + [(C_{1+2} + C_{3+4} + C_{1-4} + C_{2-3}) - (A_1 + A_2 + A_3 + A_4)](u_1 v_2 v_3 u_4 + v_1 u_2 u_3 v_4) \right\}, \quad (46)$$

where we have defined

$$C_{\mathbf{k}} = A_{\mathbf{k}} + B_{\mathbf{k}}. \quad (47)$$

The effective  $1/S$  interacting spin-wave Hamiltonian in

terms of the magnon operators reads

$$\mathcal{H}_{\text{eff}} = \sum_{\mathbf{k}} \left[ (\varepsilon_{\mathbf{k}} + \delta \varepsilon_{\mathbf{k}}) b_{\mathbf{k}}^\dagger b_{\mathbf{k}} + \frac{O_{\mathbf{k}}}{2} (b_{\mathbf{k}}^\dagger b_{-\mathbf{k}}^\dagger + b_{\mathbf{k}} b_{-\mathbf{k}}) \right] + \frac{1}{2!} \sum_{\{\mathbf{k}_i\}} V_a(b_1^\dagger b_2^\dagger b_3 + \text{H.c.}) + \frac{1}{3!} \sum_{\{\mathbf{k}_i\}} V_b(b_1^\dagger b_2^\dagger b_3^\dagger + \text{H.c.}) + \sum_{\{\mathbf{k}_i\}} V_c b_1^\dagger b_2^\dagger b_3 b_4. \quad (48)$$

At zero temperature the bare magnon propagator is defined as

$$G_0^{-1}(\mathbf{k}, \omega) = \omega - \varepsilon_{\mathbf{k}} + i0^+. \quad (49)$$

The first order  $1/S$  correction to the magnon energy is determined by the Dyson equation

$$\omega - \varepsilon_{\mathbf{k}} - \Sigma(\mathbf{k}, \omega) = 0, \quad (50)$$

with the one-loop self-energy  $\Sigma(\mathbf{k}, \omega) = \Sigma_a(\mathbf{k}, \omega) + \Sigma_b(\mathbf{k}, \omega) + \Sigma_c(\mathbf{k})$ , where  $\Sigma_c(\mathbf{k}) = \delta\varepsilon_{\mathbf{k}}$  is a frequency-independent Hartree-Fock correction, while  $\Sigma_{a,b}(\mathbf{k}, \omega)$  are calculated as

$$\Sigma_a(\mathbf{k}, \omega) = \frac{1}{2} \sum_{\mathbf{p}} \frac{|V_a(\mathbf{p}, \mathbf{k} - \mathbf{p}; \mathbf{k})|^2}{\omega - \varepsilon_{\mathbf{p}} - \varepsilon_{\mathbf{k}-\mathbf{p}} + i0^+}, \quad (51)$$

$$\Sigma_b(\mathbf{k}, \omega) = -\frac{1}{2} \sum_{\mathbf{p}} \frac{|V_b(\mathbf{p}, -\mathbf{k} - \mathbf{p}, \mathbf{k})|^2}{\omega + \varepsilon_{\mathbf{p}} + \varepsilon_{\mathbf{k}+\mathbf{p}} - i0^+}. \quad (52)$$

The on-shell solution consists of setting  $\omega = \varepsilon_{\mathbf{k}}$  in the self-energy (51) and (52) leads to the following expression for the  $1/S$  renormalized spectrum

$$\omega_{\mathbf{k}} \equiv \bar{\omega}_{\mathbf{k}} - i\Gamma_{\mathbf{k}} = \varepsilon_{\mathbf{k}} + \Sigma(\mathbf{k}, \varepsilon_{\mathbf{k}}), \quad (53)$$

where  $\bar{\omega}_{\mathbf{k}} = \text{Re}[\omega_{\mathbf{k}}]$  is the renormalized spin-wave energy and  $\Gamma_{\mathbf{k}} = -\text{Im}[\omega_{\mathbf{k}}]$  represents the magnon decay rate. We then plot the  $1/S$  LSWT dispersion of  $\text{Cs}_2\text{CuCl}_4$  [27] in Fig. 3.

#### IV. TORQUE EQUILIBRIUM SPIN WAVE THEORY

Zero-point quantum fluctuation in a non-collinear ordered spin structure can lead to deviations in the measured ordering wavevector compared to the classical one. The correction emerging from the spin Casimir effect is usually neglected, but it was recently shown that this not a bonafide assumption. In Du *et. al.* [28, 29] it was clearly established that in certain situations a standard spin wave theory is no longer applicable due to the spin Casimir quantum effect, even when the system is long-range ordered. A important consequence of these quantum fluctuations is on the spiral state which can become unstable, which is different from the case of long-range-order melting. As mentioned earlier the classical signatures of this instabilities are the divergences of the ordering wave vector at the quantum critical point and the strongly singular one-loop expansions of the energy spectrum and the sublattice magnetization. In this section we extend the applicability of the TESWT formalism to include the effects of DM interaction in an anisotropic TLAF. Using INS experimental data from  $\text{Cs}_2\text{CuCl}_4$ , we obtain fitting parameters for the exchange constants and DM interactions utilized in subsequent indirect  $K$ -edge RIXS calculations.

##### A. TESWT formalism

Spin Casimir effect will change the classical ground state to a new saddle point. This new ground state can be unambiguously determined once we compute the value of  $\mathbf{Q}$ . An

ordinary approach is considering the  $1/S$  correction  $\Delta Q$ , as we show in Sec. III B. However, such method gives an unphysical result, see Fig. 2. As  $\alpha \rightarrow 2$ , the  $1/S$  correction  $\Delta Q$  becomes infinites. In this paper, we use TESWT [28, 29] and generalize the formulation to include DM interactions. The basic idea of TESWT is still to minimize the energy of ground state. The spin Casimir torque is defined as

$$\mathbf{T}_{sc}(\mathbf{Q}) = \sum_{\mathbf{k}} \left\langle \Psi_{vac} \left| \frac{\partial H_{sw}}{\partial \mathbf{Q}} \right| \Psi_{vac} \right\rangle, \quad (54)$$

where  $|\Psi_{vac}\rangle$  represents the quasiparticle vacuum state. Then the torque equilibrium condition is

$$\begin{aligned} \mathbf{T}_{sc}(\mathbf{Q}) + \mathbf{T}_{cl}(\mathbf{Q}) &= \sum_{\mathbf{k}} \left\langle \Psi_{vac} \left| \frac{\partial (H_{sw} + H_{cl})}{\partial \mathbf{Q}} \right| \Psi_{vac} \right\rangle = 0, \\ \mathbf{T}_{sc}(\mathbf{Q}_{cl}) &= \frac{3JS}{2} \sum_{\mathbf{k}} \frac{A_{\mathbf{k}} - B_{\mathbf{k}}}{\varepsilon_{\mathbf{k}}} \frac{\partial \gamma_{\mathbf{k}+\mathbf{Q}}}{\partial \mathbf{Q}} \Big|_{\mathbf{Q}_{cl}}, \\ \mathbf{T}_{cl}(\mathbf{Q}) &= 3NJS^2 \frac{\partial \gamma_{\mathbf{Q}}}{\partial \mathbf{Q}}, \quad \mathbf{T}_{cl}(\mathbf{Q}_{cl}) = 0, \end{aligned} \quad (55)$$

where  $\mathbf{Q}$  is the final ordering vector,  $H_{cl} = E_0(\mathbf{Q})$  is the classical energy. With the fact that the spin-wave spectrum function  $\varepsilon_{\mathbf{k}}$  is only well defined at  $\mathbf{Q}_{cl}$ , we try to find a system whose classical ordering vector is  $\mathbf{Q}$  for convenience of calculation. Thus we shift the function depending on classical ordering vector  $\mathbf{Q}_{cl}$  to  $\mathbf{Q}$  by

$$H_2(\alpha, \eta, \mathbf{Q}) = \tilde{H}_2(\tilde{\alpha}, \tilde{\eta}, \mathbf{Q}) + H_2^c, \quad (56)$$

$$A_{\mathbf{k}} = \tilde{A}_{\mathbf{k}} + A_{\mathbf{k}}^c, \quad B_{\mathbf{k}} = \tilde{B}_{\mathbf{k}} + B_{\mathbf{k}}^c, \quad (57)$$

where  $\tilde{H}_2, \tilde{A}_{\mathbf{k}}$  and  $\tilde{B}_{\mathbf{k}}$  are functions of another spin system whose classical ordering vector  $\tilde{\mathbf{Q}}_{cl}$  equals  $\mathbf{Q}$ . We have many combinations of  $(\tilde{\alpha}, \tilde{\eta})$  that satisfy this condition. As  $\eta/\alpha$  is small, with perturbation theory, we believe  $\tilde{\eta} = \eta$  is reasonable. Thus the new parameters are given by,

$$\begin{cases} \tilde{\alpha} = -2 \cos \frac{Q}{2} - \eta \cot \frac{Q}{2}, \\ \tilde{\eta} = \eta. \end{cases} \quad (58)$$

The spin Casimir torque is then expressed approximately as  $\mathbf{T}_{sc}(\mathbf{Q}) = \tilde{\mathbf{T}}_{sc}(\mathbf{Q})$ . Thus the torque equilibrium equation in Eq. (55) can be written as

$$\frac{\partial \gamma_{\mathbf{Q}}}{\partial \mathbf{Q}} = -\frac{1}{2NS} \sum_{\mathbf{k}} \frac{\tilde{A}_{\mathbf{k}} - \tilde{B}_{\mathbf{k}}}{\tilde{\varepsilon}_{\mathbf{k}}} \cdot \frac{\partial \tilde{\gamma}_{\mathbf{k}+\mathbf{Q}}}{\partial \mathbf{Q}}. \quad (59)$$

Now the exchange parameters on the left-hand side of the equation are exact as  $\alpha, \eta$ . While the parameters on the right-hand side approximate as  $\tilde{\alpha} = -2 \cos \frac{Q}{2} - \eta \cot \frac{Q}{2}$ . We solve this equation numerically and give the results in Fig. 2. If there is no DM interaction, TESWT gives  $Q = 2\pi$  for  $\alpha \geq 1.2$ , which are similar to the results of numerical methods [18, 30]. The LSWT, however, giving a wider region for spiral order phase, can't describe the region for  $1.2 \leq \alpha \leq 2$ . As anticipated, a little DM interaction,  $\eta = 0.05$ , changes our final ordering vector obviously. The DM interaction can improve the stabilization of spiral order and enlarge its region.

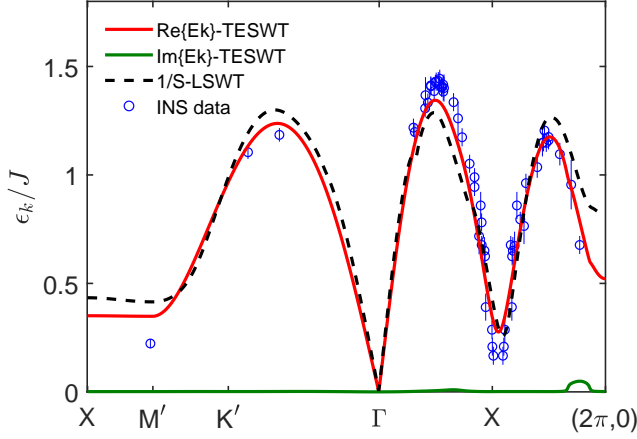


FIG. 3. Magnon dispersion  $\epsilon_{\mathbf{k}}$  within TESWT and 1/S-LSWT approach. The red line is fitted by TESWT with  $\alpha = 0.316$  and  $\eta = 0.025$  ( $J = 0.480(9)\text{meV}$ ). The circles are experimental data of inelastic neutron scattering for  $\text{Cs}_2\text{CuCl}_4$  [44]. The black dashed line is the fitting result of 1/S-LSWT with  $\alpha = 0.417$  and  $\eta = 0.021$  ( $J = 0.573(9)\text{meV}$ ). The energies of all results are divided by  $J = 0.480\text{ meV}$  as ordinate. The momentum points in the path are defined in Fig. 1.

We then diagonalize  $\tilde{H}_2(\tilde{\alpha}, \tilde{\eta}, \mathbf{Q})$  and treat  $H_2^c$  as a counterterm. For simplification, we neglect  $H_3^c$  and  $H_4^c$  and write the Hamiltonian as

$$\tilde{H}_{sw} = \tilde{H}_2 + H_2^c + \tilde{H}_3 + \tilde{H}_4. \quad (60)$$

Following the same procedure described in Sec. III, the effective Hamiltonian now reads

$$\begin{aligned} \tilde{\mathcal{H}}_{\text{eff}} = & \sum_{\mathbf{k}} \left[ (\tilde{\epsilon}_{\mathbf{k}} + \delta\tilde{\epsilon}_{\mathbf{k}}) b_{\mathbf{k}}^\dagger b_{\mathbf{k}} + \frac{\tilde{O}_{\mathbf{k}}}{2} (b_{\mathbf{k}}^\dagger b_{-\mathbf{k}}^\dagger + b_{\mathbf{k}} b_{-\mathbf{k}}) \right. \\ & + \tilde{\epsilon}_{\mathbf{k}}^c b_{\mathbf{k}}^\dagger b_{\mathbf{k}} + \frac{O_{\mathbf{k}}^c}{2} (b_{\mathbf{k}}^\dagger b_{-\mathbf{k}}^\dagger + b_{\mathbf{k}} b_{-\mathbf{k}}) \left. \right] \\ & + \frac{1}{2!} \sum_{\{\mathbf{k}_i\}} \tilde{V}_a (b_1^\dagger b_2^\dagger b_3 + \text{H.c.}) + \frac{1}{3!} \sum_{\{\mathbf{k}_i\}} \tilde{V}_b (b_1^\dagger b_2^\dagger b_3^\dagger + \text{H.c.}) \\ & + \sum_{\{\mathbf{k}_i\}} \tilde{V}_c b_1^\dagger b_2^\dagger b_3 b_4. \end{aligned} \quad (61)$$

where  $\tilde{F}$  means  $F(\tilde{\alpha}, \tilde{\eta}, \mathbf{Q})$  ( $F$  is an arbitrary operator) and

$$\tilde{\epsilon}_{\mathbf{k}}^c = (\tilde{u}_{\mathbf{k}}^2 + \tilde{v}_{\mathbf{k}}^2) A_{\mathbf{k}}^c + 2\tilde{u}_{\mathbf{k}} \tilde{v}_{\mathbf{k}} B_{\mathbf{k}}^c = \frac{1}{\tilde{\epsilon}_{\mathbf{k}}} [\tilde{A}_{\mathbf{k}} A_{\mathbf{k}} - \tilde{B}_{\mathbf{k}} B_{\mathbf{k}}] - \tilde{\epsilon}_{\mathbf{k}}, \quad (62)$$

$$O_{\mathbf{k}}^c = (\tilde{u}_{\mathbf{k}}^2 + \tilde{v}_{\mathbf{k}}^2) B_{\mathbf{k}}^c + 2\tilde{u}_{\mathbf{k}} \tilde{v}_{\mathbf{k}} A_{\mathbf{k}}^c = \frac{1}{\tilde{\epsilon}_{\mathbf{k}}} [\tilde{A}_{\mathbf{k}} B_{\mathbf{k}} - \tilde{B}_{\mathbf{k}} A_{\mathbf{k}}]. \quad (63)$$

In this way, we shift the classical ordering vector  $\mathbf{Q}_{cl}$  to the final ordering vector  $\mathbf{Q}$  using the TESWT. Everything is easy to repeat as we need only to consider  $H_2^c$  and  $\mathbf{Q}$  from TESWT.

Therefore, the first order 1/S corrected dispersion of magnon is now changed to

$$\omega_{\mathbf{k}} = \tilde{\epsilon}_{\mathbf{k}} + \tilde{\epsilon}_{\mathbf{k}}^c + \delta\tilde{\epsilon}_{\mathbf{k}} + \tilde{\Sigma}_3^a(\mathbf{k}, \tilde{\epsilon}_{\mathbf{k}}) + \tilde{\Sigma}_3^b(\mathbf{k}, \tilde{\epsilon}_{\mathbf{k}}), \quad (64)$$

TABLE I. Parameter values of  $\text{Cs}_2\text{CuCl}_4$  using different methods. The first line is our TESWT fit results. The second line is our 1/S-SWT fitting parameters. The third line gives the fitting parameters of series expansion (SE) method [27]. The last line gives the parameters measured by Electron-Spin-Resonance (ESR) [49].

Method	$J(\text{meV})$	$J'(\text{meV})$	$D(\text{meV})$
TESWT	$0.480 \pm 0.009$	$0.152 \pm 0.015$	$0.012 \pm 0.002$
1/S-LSWT	$0.573 \pm 0.009$	$0.239 \pm 0.014$	$0.012 \pm 0.001$
SE	$0.374 \pm 0.005$	$0.128 \pm 0.005$	$0.020 \pm 0.002$
ESR	$0.41 \pm 0.02$	$0.122 \pm 0.006$	—

## B. INS fitting

The primary purpose of this paper is to compute the RIXS spectrum. As discussed above, with anisotropy the application of 1/S-LSWT formalism is tricky. But, application of TESWT requires magnetic interaction parameters computed within that formalism. The most direct way to do this is to compare the theoretical dispersion with the experimental data. We fit the INS data of  $\text{Cs}_2\text{CuCl}_4$  [44] to Eq. (64) using iterative least squares estimation both by TESWT and 1/S-LSWT. Our fitting parameters along with results from other sources are reported in Table. I. Our dispersion line fits are reported in Fig. 3. The absence of higher order terms within our TESWT could be a source of disagreement with the series expansion results [27]. While it maybe fruitful to investigate the above mentioned discrepancy, within the context of our RIXS calculation we do not expect the improved interaction constants to bring about much qualitative or quantitative differences. Additionally, TESWT is easier to carry out and gives the final ordering vector quickly.

## C. Sublattice magnetization

We then try to study the phase diagram of anisotropy triangular lattice. In spin system, the sublattice magnetization can describe the phase transition well. With the fact the second-order correction of the sublattice magnetization contributes little to the result, we only consider the first order of sublattice magnetization,

$$\langle S \rangle = S - \delta S_1 = S - \langle a_i^\dagger a_i \rangle, \quad (65)$$

where

$$\langle a_i^\dagger a_i \rangle = \langle a_{\mathbf{k}}^\dagger a_{\mathbf{k}} \rangle = \langle \tilde{v}_{\mathbf{k}}^2 \rangle. \quad (66)$$

In Fig. 4 we plot the sublattice magnetization  $\langle S \rangle$  variation with spatial anisotropy. Our result without DM interaction is consistent with previous numerical studies [18, 30]. Consistent with our previous analysis of Fig. 2, the spiral order is destroyed at  $\alpha \geq 1.2$ . In addition, the spiral order is unsafe at  $\alpha \leq 0.5$ , consistent with modified spin wave results [18]. We pay attention to the effect of DM interaction. The DM interaction, which comes from the spin-orbit coupling, helps

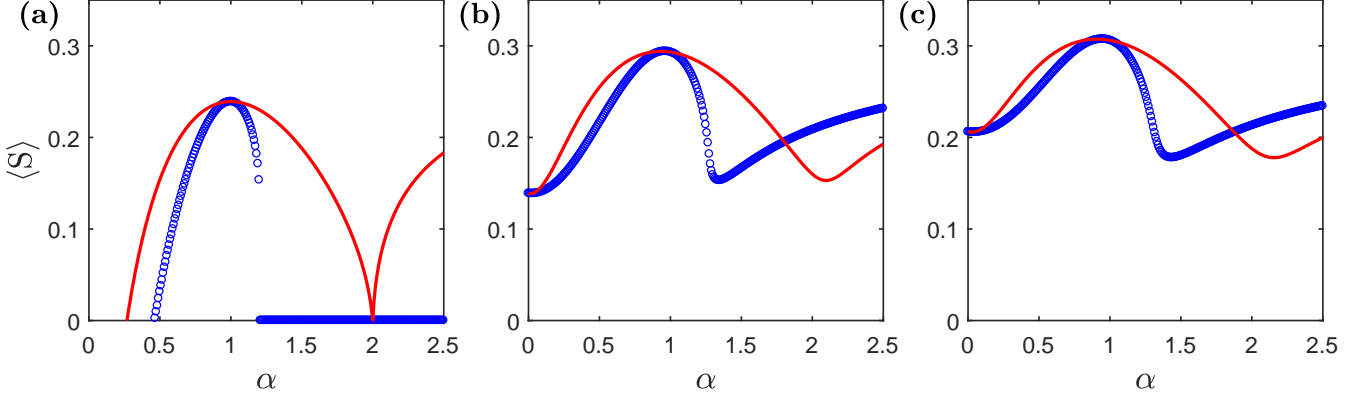


FIG. 4. Variation of sublattice magnetization  $\langle S \rangle$  with spatial anisotropy  $\alpha$ . The red (blue) solid line (circles) represents LSWT (TESWT) results. (a)  $\eta = 0$ , (b)  $\eta = 0.03$  and (c)  $\eta = 0.05$ .

to build a non-collinear spin ground state. It is evident from Fig. 4, as  $\eta$  gets bigger, the phase transformation point in the region  $\alpha \leq 0.5$  becomes smaller until disappear. And  $\alpha \geq 1.2$  also becomes safer. This means the DM interactions enlarge the region of the spiral state. Our focus in this article is on the multimagnon RIXS spectrum in the spiral phase. This implies that our choice of parameters should be limited to the corresponding phase. We find that TESWT not only gives a physical estimate of the final ordering vector, but also correctly predicts the phase diagram of an anisotropic TLAf, helping to better understand the behavior of the spiral ground state of such geometrically frustrated systems.

## V. INDIRECT RIXS SPECTRA

### A. Noninteracting bi- and trimagnon RIXS

In this section we calculate the spectra of RIXS of bi- and trimagnon. The results in this part are using TESWT while a general and concrete approach of LSWT is shown in Appendix A. The indirect RIXS scattering operator, is given by [50, 51]

$$\mathcal{R}_{\mathbf{q}} = \sum_{i,\delta} J_{i\delta} e^{i\mathbf{q} \cdot \mathbf{r}_i} \mathbf{S}_i \cdot \mathbf{S}_{i+\delta}, \quad (67)$$

where  $\mathbf{q}$  is the scattering momentum. In quasiparticle representation, the magnon creation parts of the RIXS scattering operator can be given by

$$\mathcal{R}_{\mathbf{q}} = \sum_{1+2=\mathbf{q}} \tilde{M}(1,2) b_1^\dagger b_2^\dagger + \sum_{1+2+3=\mathbf{q}} \tilde{N}(1,2,3) b_1^\dagger b_2^\dagger b_3^\dagger, \quad (68)$$

where the bimagnon scattering matrix element is

$$\begin{aligned} \tilde{M}(1,2) = \frac{3JS}{2!} \{ & [\xi_1 + \lambda_1 + \xi_2 + \lambda_2 - 2(\gamma_{\mathbf{Q}} + \xi_{\mathbf{q}})](\tilde{u}_1 \tilde{v}_2 + \tilde{v}_1 \tilde{u}_2) \\ & + (\xi_1 - \lambda_1 + \xi_2 - \lambda_2)(\tilde{u}_1 \tilde{u}_2 + \tilde{v}_1 \tilde{v}_2) \}, \end{aligned} \quad (69)$$

and the trimagnon scattering matrix element is

$$\begin{aligned} \tilde{N}(1,2,3) = \frac{3JS}{3!} i \sqrt{\frac{3}{2SN}} [ & (\tilde{\gamma}_1 - \tilde{\gamma}_{2+3} - \frac{1}{4} \tilde{\gamma}_{\mathbf{q}})(\tilde{u}_1 + \tilde{v}_1) \\ & \times (\tilde{u}_2 \tilde{v}_3 + \tilde{v}_2 \tilde{u}_3) + (\tilde{\gamma}_2 - \tilde{\gamma}_{1+3} - \frac{1}{4} \tilde{\gamma}_{\mathbf{q}})(\tilde{u}_2 + \tilde{v}_2) \\ & \times (\tilde{u}_1 \tilde{v}_3 + \tilde{v}_1 \tilde{u}_3) + (\tilde{\gamma}_3 - \tilde{\gamma}_{1+2} - \frac{1}{4} \tilde{\gamma}_{\mathbf{q}})(\tilde{u}_3 + \tilde{v}_3) \\ & \times (\tilde{u}_1 \tilde{v}_2 + \tilde{v}_1 \tilde{u}_2) ]. \end{aligned} \quad (70)$$

We neglect the corrections from magnon interactions for the trimagnon intensity, which appear at  $1/S^2$  order.

Next, using Eqs. (A4) and (A5) stated in Appendix A we obtain the following expressions for  $I_2(\mathbf{q}, \omega)$  (noninteracting bimagnon) and  $I_3(\mathbf{q}, \omega)$  (trimagnon) scattering intensity

$$I_2(\mathbf{q}, \omega) = 2 \sum_{\mathbf{k}} \tilde{M}_{\mathbf{k}+\mathbf{q},-\mathbf{k}}^2 \delta(\omega - \omega_{\mathbf{k}+\mathbf{q}}^{(0)} - \omega_{\mathbf{k}}^{(0)}), \quad (71)$$

$$I_3(\mathbf{q}, \omega) = 6 \sum_{\mathbf{k},\mathbf{p}} \tilde{N}_{\mathbf{k},\mathbf{q}-\mathbf{k}-\mathbf{p},\mathbf{p}}^2 \delta(\omega - \omega_{\mathbf{k}}^{(0)} - \omega_{\mathbf{q}-\mathbf{k}-\mathbf{p}}^{(0)} - \omega_{\mathbf{p}}^{(0)}), \quad (72)$$

where  $\omega_{\mathbf{k}}^{(0)} = \tilde{\epsilon}_{\mathbf{k}} + \epsilon_{\mathbf{k}}^c$ .

In Fig. 5 we display our results of the non-interacting bi- and tri- magnon RIXS spectra at various points across the MBZ. Overall the agreement between the two formalism is reasonable. Our TESWT result generates more peaks about the bimagnon. As discussed earlier, the TESWT is the physically correct formalism in the presence of anisotropy. We note that in the anisotropic regime  $\alpha = 1$ , our TESWT results are identical with the LSWT formalism since the final ordering vector  $\mathbf{Q}$  equals the classical vector  $\mathbf{Q}_{cl}$ , see Fig. 11.

### B. Interacting bimagnon RIXS spectra

We now proceed with the analysis of  $1/S$  correction to the two-magnon Green's function by taking into account both the self-energy correction to the single magnon propagator  $G$  according to the Dyson equation and the vertex insertions to the two-particle propagator  $\Pi$  which satisfies the Bethe-Salpeter (BS) equation [52, 53].

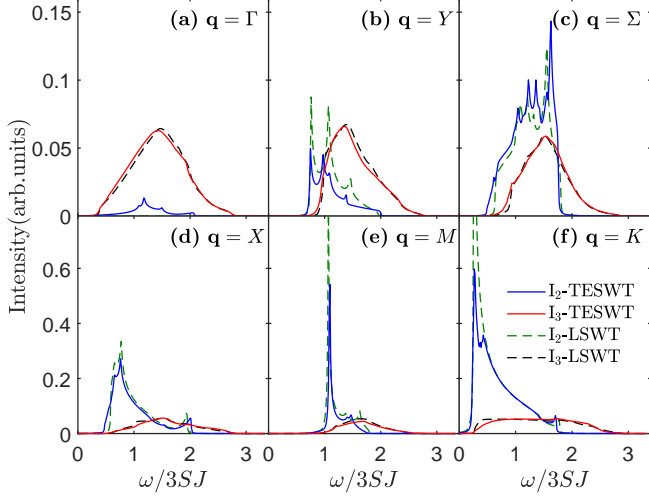


FIG. 5. Noninteracting bimagnon spectra across high symmetry MBZ points. The line plots compare results from TESWT against LSWT for  $\alpha = 0.8$  and  $\eta = 0$ .

Using the procedure outlined in our prior work [1] and Feynman rules in momentum space, we obtain the following equations for the two-particle propagator and the associated vertex function as

$$\Pi_{\mathbf{k}\mathbf{k}'}(\mathbf{q}, \omega) = 2i \int \frac{d\omega'}{2\pi} G_{\mathbf{k}+\mathbf{q}}(\omega + \omega') G_{-\mathbf{k}}(-\omega') \Gamma_{\mathbf{k}\mathbf{k}'}(\omega, \omega'), \quad (73)$$

$$\Gamma_{\mathbf{k}\mathbf{k}'}(\omega, \omega') = \delta_{\mathbf{k}\mathbf{k}'} + \sum_{\mathbf{k}_1} 2i \int \frac{d\omega_1}{2\pi} G_{\mathbf{k}_1+\mathbf{q}}(\omega + \omega_1) G_{-\mathbf{k}_1}(-\omega_1) \times \mathcal{V}_{\mathbf{k}\mathbf{k}_1}^{\text{IR}}(\omega', \omega_1) \Gamma_{\mathbf{k}_1\mathbf{k}'}(\omega, \omega_1), \quad (74)$$

where the basic one-magnon propagator up to  $1/S$  order is now given by

$$G^{-1}(\mathbf{k}, \omega) = \omega - \omega_{\mathbf{k}}^{(0)} + i0^+. \quad (75)$$

And the lowest order two-particle irreducible interaction vertex in Fig. 6(c) reads

$$\mathcal{V}_{\text{IR}} = \mathcal{V}_4 + \mathcal{V}_3^{(a)} + \mathcal{V}_3^{(b)} + \mathcal{V}_3^{(c)} + \mathcal{V}_3^{(d)}, \quad (76)$$

in which the frequency-independent four-point vertex  $\mathcal{V}_4$  coming from the quartic Hamiltonian can be written as

$$\mathcal{V}_4 = \tilde{V}_c(\mathbf{k}_1 + \mathbf{q}, -\mathbf{k}_1; \mathbf{k} + \mathbf{q}, -\mathbf{k}), \quad (77)$$

and the other four vertices  $\mathcal{V}_3^{(a-d)}$  in the same  $1/S$  order which are assembled from two three-point vertices and one

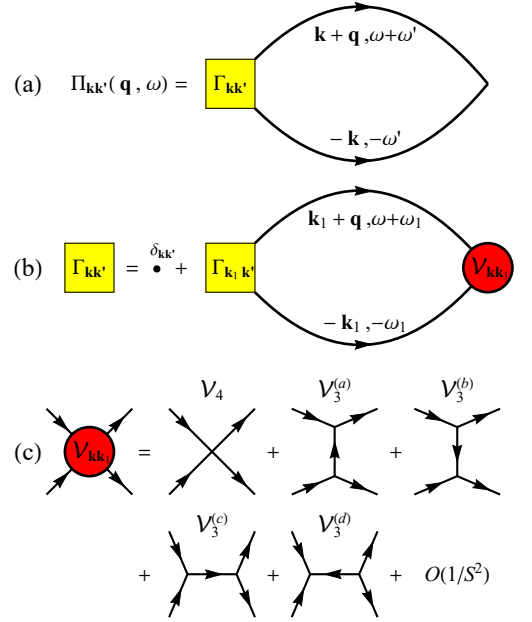


FIG. 6. Diagrammatic representation for the two-magnon interactions. (a) Two-magnon propagator  $\Pi_{\mathbf{k}\mathbf{k}'}(\mathbf{q}, \omega)$ , (b) Bethe-Salpeter equation of the vertex function  $\Gamma_{\mathbf{k}\mathbf{k}'}(\omega, \omega')$  and (c) the  $1/S$  order irreducible interaction  $\mathcal{V}_{\text{IR}}$ . Solid lines with an arrow in (a) and (b) stand for the single-magnon propagators. The total irreducible bimagnon scattering vertices can be classified into - direct ( $\mathcal{V}_4$ ) and indirect ( $\mathcal{V}_3^{a-d}$ ) contributions. Note, the direct ladder interaction leads to a stable magnon interaction event, but the indirect collision process has contributions from virtual decays and recombination.

frequency-dependent propagator can be written as

$$\mathcal{V}_3^{(a)} = \frac{1}{(2!)^2} [\tilde{V}_a(\mathbf{k}_1 + \mathbf{q}, \mathbf{k} - \mathbf{k}_1; \mathbf{k} + \mathbf{q}) G_0(\mathbf{k} - \mathbf{k}_1, \omega' - \omega_1) \times \tilde{V}_a^*(-\mathbf{k}, \mathbf{k} - \mathbf{k}_1; -\mathbf{k}_1)], \quad (78)$$

$$\mathcal{V}_3^{(b)} = \frac{1}{(2!)^2} [\tilde{V}_a^*(\mathbf{k} + \mathbf{q}, \mathbf{k}_1 - \mathbf{k}; \mathbf{k}_1 + \mathbf{q}) G_0(\mathbf{k}_1 - \mathbf{k}, \omega_1 - \omega') \times \tilde{V}_a(-\mathbf{k}_1, \mathbf{k}_1 - \mathbf{k}; -\mathbf{k})], \quad (79)$$

$$\mathcal{V}_3^{(c)} = \frac{1}{(2!)^2} [\tilde{V}_a(\mathbf{k}_1 + \mathbf{q}, -\mathbf{k}_1; \mathbf{q}) G_0(\mathbf{q}, \omega) \times \tilde{V}_a^*(\mathbf{k} + \mathbf{q}, -\mathbf{k}; \mathbf{q})], \quad (80)$$

$$\mathcal{V}_3^{(d)} = \frac{1}{(3!)^2} [\tilde{V}_b(\mathbf{k}_1 + \mathbf{q}, -\mathbf{k}_1, -\mathbf{q}) G_0(-\mathbf{q}, -\omega) \times \tilde{V}_b^*(\mathbf{k} + \mathbf{q}, -\mathbf{k}, -\mathbf{q})], \quad (81)$$

where we have retained only the bare propagator  $G_0$  for each intermediate line in  $\mathcal{V}_3^{(a-d)}$  in the spirit of  $1/S$  expansion. Note, the vertex expressions here are different from those stated within the traditional  $1/S$ -SWT approach [1]. The vertex expressions here are shifted by the correct TESWT wave vector. Based on the above generalization, we now derive the final solution of the interacting RIXS intensity from the ladder approximation BS equation.

We adopt a numerical approach to compute the interacting bimagnon RIXS intensity. We assume that two on-shell

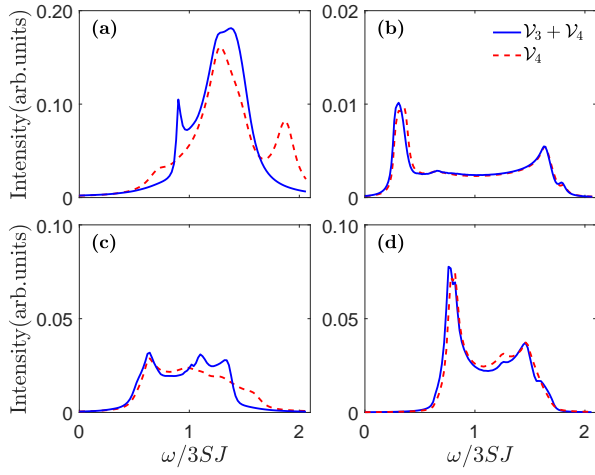


FIG. 7. Interacting bimagnon RIXS intensity at  $\mathbf{q} = Y(0, \pi/\sqrt{3})$  point with (a)  $\alpha = 1, \eta = 0$ , (b)  $\alpha = 0.316, \eta = 0.025$ , (c)  $\alpha = 0.7, \eta = 0$  and (d)  $\alpha = 0.7, \eta = 0.05$ .

magnons are created and annihilated in the repeated ladder scattering process with  $\omega' \approx -\omega_{\mathbf{k}}^{(0)} = -\tilde{\varepsilon}_{\mathbf{k}} - \varepsilon_{\mathbf{k}}^c$  and  $\omega_1 \approx -\omega_{\mathbf{k}_1}^{(0)} = -\tilde{\varepsilon}_{\mathbf{k}_1} - \varepsilon_{\mathbf{k}_1}^c$ . We substitute (73) and (74) into (A6) to obtain

$$\chi_2 = \sum_{\mathbf{k}\mathbf{k}'} \tilde{M}_{\mathbf{k}} \tilde{M}_{\mathbf{k}'} [\delta_{\mathbf{k}\mathbf{k}'} \Pi_{\mathbf{k}} + \Pi_{\mathbf{k}} \sum_{\mathbf{k}_1} V_{\mathbf{k}\mathbf{k}_1} \Pi_{\mathbf{k}_1} \Pi_{\mathbf{k}_1\mathbf{k}'}], \quad (82)$$

where  $\Pi_{\mathbf{k}} = 2[\omega - \omega_{\mathbf{k}+\mathbf{q}} - \omega_{\mathbf{k}} + i0^+]^{-1}$  is the renormalized two-magnon propagator in the absence of vertex correction. To proceed further we divide the BZ into  $N$  points and replace the continuous momenta  $(\mathbf{k}, \mathbf{k}', \mathbf{k}_1)$  with discrete variables  $(m, n, l)$ . Thus, we can write

$$\hat{\chi}_{mn} = \tilde{M}_m \tilde{M}_n [\delta_{mn} \Pi_m + \Pi_m \sum_l V_{ml} \Pi_l \Gamma_{ln}]. \quad (83)$$

where

$$\Gamma_{mn} = \delta_{mn} + \sum_l \Pi_l V_{ml} \Gamma_{ln}. \quad (84)$$

Adopting the matrix notation  $\Gamma = (\hat{1} - \mathbf{V}\Pi)^{-1}$  we obtain the final form of the  $\hat{\chi}$  matrix as

$$\hat{\chi}^T = \hat{\mathcal{D}}[\hat{1} - \hat{\Gamma}]^{-1} \hat{\mathcal{G}}, \quad (85)$$

where we have defined the following  $N \times N$  matrices,

$$\hat{\mathbf{I}}_{mn} = \delta_{mn}, \hat{\mathcal{D}}_{mn} = \delta_{mn} \tilde{M}_m, \quad (86)$$

$$\hat{\Gamma}_{mn} = \Pi_m V_{mn}, \hat{\mathcal{G}}_{mn} = \delta_{mn} \Pi_m \tilde{M}_n. \quad (87)$$

The interacting bimagnon RIXS susceptibility is computed as

$$\chi_2(\mathbf{q}, \omega) = \sum_{m,n} \hat{\chi}_{mn}. \quad (88)$$

We use Eqs. (73) - (88) and Eq. (A4) stated in Appendix A to numerically compute our interacting bimagnon RIXS intensity at  $M, M'$ , and  $Y$  MBZ points.

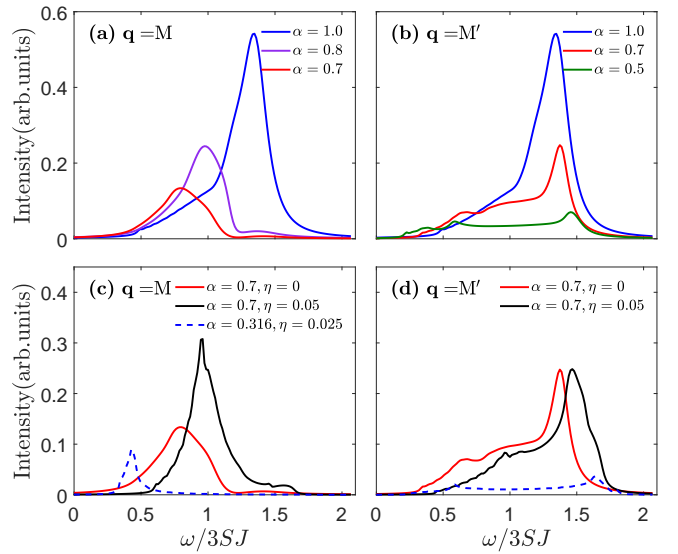


FIG. 8. Influence of spatial anisotropy and DM interaction on the interacting bimagnon intensity at two different roton points  $M(0, 2\pi/\sqrt{3})$  and  $M'(\pi, \pi/\sqrt{3})$ . The first row shows the effect of spatial anisotropy. The second row is the influence of DM interaction. The dashed line utilizes TESWT fitting parameters for  $\text{Cs}_2\text{CuCl}_4$ .

In Fig. 7 we show the spectra at the  $Y$  point. The first panel is a reproduction of our previous result reported in Ref. 1. In Fig. 7(b) we display the result of TESWT  $\text{Cs}_2\text{CuCl}_4$  RIXS. Compared to the isotropic case or to the other anisotropic situations, panels (c) and (d), this spectrum is substantially broadened. With increasing anisotropy the lattice can be envisioned as disintegrating into a set of loosely coupled chains. Thus, instead of bimagnons one can expect the emergence of spinons as is expected in 1d systems. 1d RIXS has been able to capture multi-spinon excitations [54, 55]. Thus, this RIXS spectrum feature could be used to confirm this feature reported in  $\text{Cs}_2\text{CuCl}_4$  [56]. In Fig. 7(c) or (d) we can compare the effects of including a tiny DM interaction. We find that there is a prominent low energy peak with a relatively muted higher energy response. This tiny DM interaction does not bring about any spectral down- or up- shift. The spectral weight is simply redistributed.

### C. RIXS signatures at roton points

In Fig. 8 we display the interacting RIXS intensity variation at the two anisotropic roton points  $\mathbf{q} = M$  and  $\mathbf{q} = M'$  with varying lattice anisotropy and DM interaction. The anisotropy parameter choices ensure that the TLAf does not decouple into a set of loosely coupled 1d chains, where the bosonization description has been shown to apply [56]. In the upper panel, Figs. 8(a) and 8(b), results are for zero DM interaction. Note, the two spectrum coincide in the isotropic limit since the two points are equivalent due to  $C_{3v}$  symmetry of the isotropic triangular lattice [1], while they evolve differently in the presence of spatial anisotropy. In particular, we find that

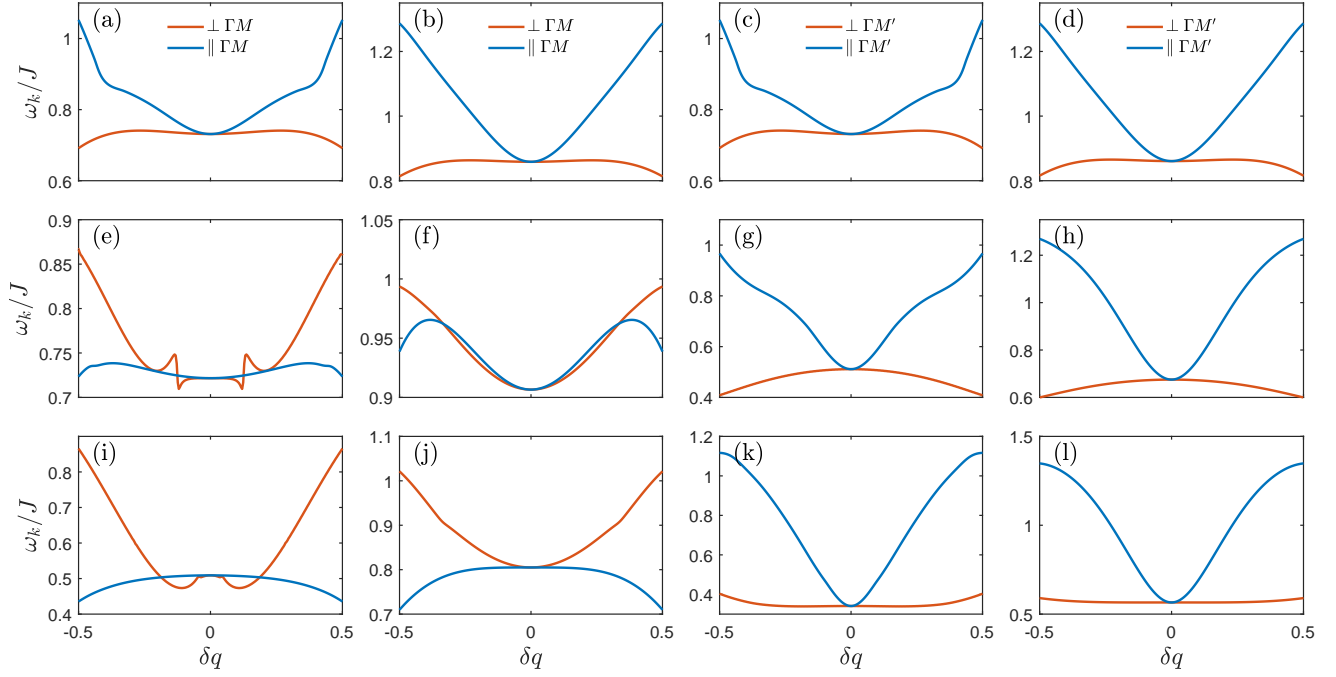


FIG. 9. The evolution of the roton minimum at  $M$  (the first two columns) and  $M'$  (the last two columns) points for the  $S = \frac{1}{2}$  spiral antiferromagnet on the triangular lattice with (the first and third column)  $\eta = 0$  and (the second and fourth column)  $\eta = 0.05$ . (a)-(d)  $\alpha = 1$ , (e)-(h)  $\alpha = 0.7$ , (i)-(l)  $\alpha = 0.5$ . The abscissa is defined as  $\Delta Q = \frac{2\pi}{3}\delta q$  for parallel to  $\Gamma M$  and  $\Delta Q = \frac{2\pi}{\sqrt{3}}\delta q$  for perpendicular to  $\Gamma M$ , so as  $\Gamma M'$ .

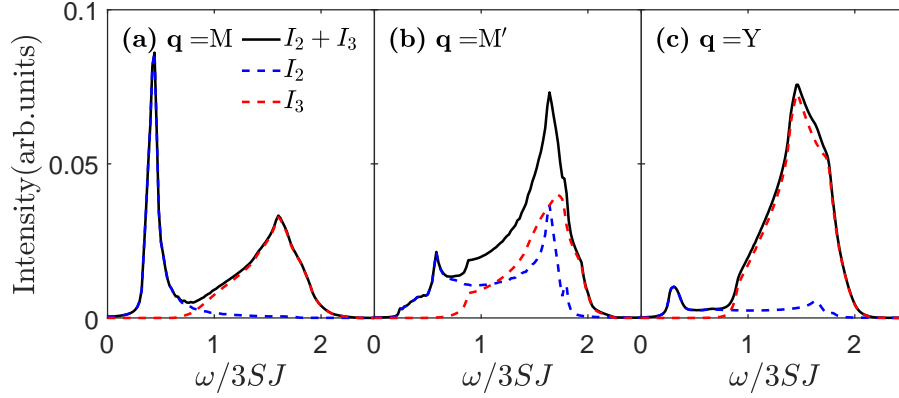


FIG. 10. Total indirect RIXS spectra  $I_2 + I_3$  (black solid line) at  $\mathbf{q} = M(0, 2\pi/\sqrt{3})$ ,  $\mathbf{q} = M'(\pi, \pi/\sqrt{3})$  and  $\mathbf{q} = Y(0, \pi/\sqrt{3})$  with TESWT fitting parameters  $\alpha = 0.316, \eta = 0.025$ . The individual interacting bimagnon spectra  $I_2$  (blue dashed line) and non-interacting tri-magnon spectra  $I_3$  (red dashed line) contributions are shown.

the roton spectra at  $\mathbf{q} = M$  point (the roton point along the  $k_y$  direction in MBZ) is very sensitive to anisotropy. Though the single-peak structure is stable against  $J'/J$ , the peak position undergoes a spectral downshift with increased anisotropy. On the other hand, for the  $q = M'$  point (along the diagonal MBZ direction), the spectra are not so sensitive, namely the peak position does not change so much in the presence of anisotropy.

In the lower panel, Figs. 8(c) and (d), we display the behavior of the RIXS spectra with DM interaction. Contrary to the isotropic case, the presence of DM interaction introduces

a spectral upshift at both  $\mathbf{q} = M$  and  $\mathbf{q} = M'$ . This could be understood by the fact that DM interaction introduces a gap, thus it requires more energy to create a bimagnon excitation. The dashed line in the lower panel is the result of realistic fit parameters generated from  $\text{Cs}_2\text{CuCl}_4$  INS data fit based on TESWT.

To gain insight into the roton behavior of the RIXS spectra we track the evolution of the roton dispersion along  $\Gamma \rightarrow M$  and  $M'$ , both parallel and perpendicular to the MBZ path, see Fig. 9. A bimagnon excitation requires  $\omega_{\mathbf{k}+\mathbf{q}} + \omega_{\mathbf{k}}$  amount energy. We notice that the one magnon dispersion along  $M$  is

more sensitive compared to that along  $M'$ . The asymmetrical sensitivity to the dispersion stiffness explains the origins of the differing roton RIXS spectra behavior. Increasing anisotropy reduces the one magnon energy near  $M$  point (the first column in Fig. 9), thus leading to a spectral downshift in Fig. 8. Whereas for the  $M'$  point, the overall energy scale of the dispersion is not affected (the third column in Fig. 9). Thus, the spectrum holds steady without any shift. However, DM interaction increases the one magnon energy both near  $M$  and  $M'$  points (the second and fourth column in Fig. 9), introducing a spectral upshift.

The evolution of the spectral height in Fig. 8 can also be explained. As anisotropy weakens the coupling between the TLAF spins to make it like a quasi-1d spin chain, it is more difficult to create a bimagnon excitation. In RIXS, this will cause a decrease in the value of the bimagnon scattering matrix element,  $|\tilde{M}(\mathbf{k} + \mathbf{q}, -\mathbf{k})|$ , in turn leading to a reduction in the spectral weight, see Fig. 8(a) and (b). On the contrary, the presence of the DM interaction encourages interactions beyond the traditional Heisenberg type. Thus, it assists with the creation of bimagnons, see Fig. 8(c), where the spectral weight increases. But for the  $\mathbf{q} = M'$  point, the weight is not sensitive to the DM interaction.

#### D. Total RIXS

In Fig. 10 we report the total RIXS spectrum for  $\text{Cs}_2\text{CuCl}_4$  with TESWT fitting parameters. The total RIXS spectrum comprises of the bi- and trimagnon response. We use Eqs. (A4) and (A5) to compute the spectrum. The interacting bimagnon (Eq. (88)) and noninteracting trimagnon intensity (Eq. (72)) are summed over to get the total RIXS spectrum. As expected, the trimagnon peak is located at a higher energy than the bimagnon response. In the response for the  $M$  and  $Y$  points, the main peaks are separated, see Figs. 10(a) and 10(c). At the  $M'$  point in Fig. 10(b), a small bimagnon peak is obvious while the main peaks of bi- and trimagnon are mixed. These observations should be helpful in distinguishing the contributions of the two different multimagnon excitations.

### VI. CONCLUSION

Due to the possible realization of various unusual ordered or disordered phases, frustrated magnetism is an active area of research in condensed matter physics [57]. Traditionally, information on the magnetic ground state and single magnon excitations is inferred from inelastic neutron scattering (INS) experiments [41, 58]. However, with the advent of RIXS spectroscopy experimentalists now have a probe that can comprehensively investigate a wide range of energy and momentum values in MBZ.

In this article we have successfully demonstrated the application of a recently proposed spin-wave theory scheme called TESWT to indirect  $K$ -edge RIXS to appropriately account

for zero-point quantum fluctuations that manifest as the emergence of spin Casimir effect in the noncollinear spin spiral state. We calculated the phase diagram with a range of parameters to demonstrate that we have the correct physical choices. As highlighted in the paper it is not a trivial matter to ensure that the sanctity of the spin spiral state is preserved. We performed a TESWT fitting of  $\text{Cs}_2\text{CuCl}_4$  INS data, which gives  $\alpha \approx 0.316$  and  $\eta \approx 0.025$ . Using these realistic parameter set we computed the indirect  $K$ -edge RIXS spectra computed within the TESWT formalism. Our results allow us to confirm that in contrast to the isotropic model, quantum fluctuations in the noncollinear anisotropic Heisenberg triangular lattice antiferromagnet can generate divergent fluctuations with drastic effects on the magnetic phase diagram. We studied the evolution of the RIXS spectra for a range of spatial anisotropy and DM interaction parameters. We find that the spectra is influenced with the occurrence of two inequivalent rotonlike points,  $M(0, 2\pi/\sqrt{3})$  and  $M'(\pi, \pi/\sqrt{3})$ . While the roton RIXS spectra at the  $M$  point undergoes a spectral downshift with increasing anisotropy, the peak at the  $M'$  is not affected. However, the peak at  $M'$  does not exhibit any downshift. Finally, we find that in the total RIXS spectra, the features of the bimagnon and the trimagnon are certainly different and easily distinguished.

In conclusion, our theoretical investigation of the indirect RIXS intensity in the spiral antiferromagnets on the anisotropic triangular lattice demonstrates that RIXS has the potential to probe and provide a comprehensive characterization of the dispersive bimagnon and trimagnon excitations in the TLAF across the entire BZ, which is far beyond the capabilities of traditional low-energy optical techniques [39, 40, 59, 60].

### ACKNOWLEDGMENTS

We thank Radu Coldea for sharing with us the INS data for  $\text{Cs}_2\text{CuCl}_4$ . T. D. acknowledges invitation, hospitality, and kind support from Sun Yat-Sen University Grant No. OEMT-2017-KF-06. T. D. acknowledges funding support from Augusta University Scholarly Activity Award. S. J., C. L. and D. X. Y. are supported by NKRDPC Grants No. 2018YFA0306001, No. 2017YFA0206203, NSFC-11574404, NSFC-2015A030313176, National Supercomputer Center in Guangzhou, and Leading Talent Program of Guangdong Special Projects.

#### Appendix A: Isotropic TLAF RIXS spectra

In this Appendix we compare the results of LSWT and TESWT for the isotropic lattice. A general approach of linear spin wave theory are applied to the calculation of indirect RIXS spectra here. After ordinary HP and Bogoliubov transformations, the magnon creation parts of the RIXS scattering

operator can be expressed as

$$\mathcal{R}_{\mathbf{q}} = \sum_{1+2=\mathbf{q}} M(1,2)b_1^\dagger b_2^\dagger + \sum_{1+2+3=\mathbf{q}} N(1,2,3)b_1^\dagger b_2^\dagger b_3^\dagger, \quad (\text{A1})$$

where the bimagnon and trimagnon scattering matrix element expression are given by

$$M(1,2) = \frac{3JS}{2!} \left\{ [\xi_1 + \lambda_1 + \xi_2 + \lambda_2 - 2(\gamma_{\mathbf{Q}} + \xi_{\mathbf{q}})](u_1 v_2 + v_1 u_2) + (\xi_1 - \lambda_1 + \xi_2 - \lambda_2)(u_1 u_2 + v_1 v_2) \right\}, \quad (\text{A2})$$

$$N(1,2,3) = \frac{3JS}{3!} i \sqrt{\frac{3}{2SN}} \left[ (\bar{\gamma}_1 - \bar{\gamma}_{2+3} - \frac{1}{4}\bar{\gamma}_{\mathbf{q}})(u_1 + v_1) \times (u_2 v_3 + v_2 u_3) + (\bar{\gamma}_2 - \bar{\gamma}_{1+3} - \frac{1}{4}\bar{\gamma}_{\mathbf{q}})(u_2 + v_2) \times (u_1 v_3 + v_1 u_3) + (\bar{\gamma}_3 - \bar{\gamma}_{1+2} - \frac{1}{4}\bar{\gamma}_{\mathbf{q}})(u_3 + v_3) \times (u_1 v_2 + v_1 u_2) \right]. \quad (\text{A3})$$

Note that all the coefficients and functions are defined at the classical ordering vector  $\mathbf{Q}_{cl}$  in LSWT.

The frequency- and momentum-dependent magnetic scattering intensity is related to the multimagnon RIXS response function via the fluctuation-dissipation theorem

$$I(\mathbf{q}, \omega) = -\frac{1}{\pi} \text{Im}[\chi_{\text{RIXS}}(\mathbf{q}, \omega)], \quad (\text{A4})$$

where the total indirect  $K$ -edge RIXS susceptibility is given by

$$\chi_{\text{RIXS}}(\mathbf{q}, \omega) = \chi_2(\mathbf{q}, \omega) + \chi_3(\mathbf{q}, \omega), \quad (\text{A5})$$

where  $\chi_2(\mathbf{q}, \omega)$  could be either a non-interacting or interacting two-magnon susceptibility, but  $\chi_3(\mathbf{q}, \omega)$  is the

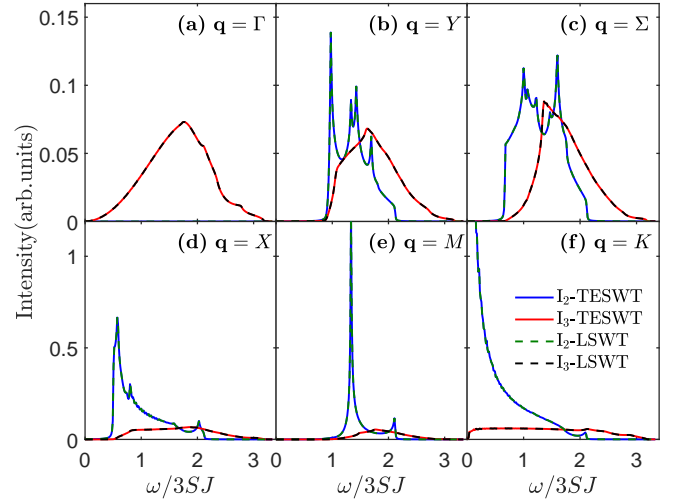


FIG. 11. Noninteracting bimagnon spectra without spatial anisotropy or DM interaction. The line plots compare results from TESWT against LSWT for  $J'/J = 1, D/J = 0$ . The curves of TESWT completely coincide with those of LSWT.

non-interacting three-magnon susceptibility. The susceptibilities can be expressed explicitly from the corresponding multi-magnon Green's function defined as

$$\chi_2(\mathbf{q}, \omega) = \sum_{\mathbf{k}\mathbf{k}'} M_{\mathbf{k}} M_{\mathbf{k}'} \Pi_{\mathbf{k}\mathbf{k}'}(\mathbf{q}, \omega), \quad (\text{A6})$$

$$\chi_3(\mathbf{q}, \omega) = \sum_{\mathbf{k}\mathbf{p}; \mathbf{k}'\mathbf{p}'} N_{\mathbf{k}, \mathbf{p}} N_{\mathbf{k}', \mathbf{p}'} \Lambda_{\mathbf{k}\mathbf{p}; \mathbf{k}'\mathbf{p}'}(\mathbf{q}, \omega), \quad (\text{A7})$$

where  $\Pi$  and  $\Lambda$  are denoted as the bimagnon and trimagnon propagator, respectively. The momentum-dependent two-magnon and three-magnon Green's function in terms of Bogoliubov quasiparticles are defined as

$$i\Pi_{\mathbf{k}\mathbf{k}'}(\mathbf{q}, t) = \langle \mathcal{T} b_{\mathbf{k}+\mathbf{q}}(t) b_{-\mathbf{k}}(t) b_{\mathbf{k}'+\mathbf{q}}^\dagger b_{-\mathbf{k}'}^\dagger \rangle, \quad (\text{A8})$$

$$i\Lambda_{\mathbf{k}\mathbf{p}; \mathbf{k}'\mathbf{p}'}(\mathbf{q}, t) = \langle \mathcal{T} b_{\mathbf{k}}(t) b_{\mathbf{q}-\mathbf{k}-\mathbf{p}}(t) b_{\mathbf{p}}(t) b_{\mathbf{k}'}^\dagger b_{\mathbf{q}-\mathbf{k}'-\mathbf{p}'}^\dagger b_{\mathbf{p}'}^\dagger \rangle, \quad (\text{A9})$$

where  $\mathcal{T}$  is the time-ordering operator and  $\langle \cdot \rangle$  is the average of the ground state. Using Eq. (A8) and Eq. (A9), we can compute the noninteracting and the interacting RIXS spectra. The non-interacting spectrum can be calculated by applying Wick's theorem to Eq. (A8) and Eq. (A9). The final expressions are stated in Eqs. (71) and (72).

- 
- [1] Cheng Luo, Trinanjan Datta, Zengye Huang, and D. X. Yao, "Signatures of indirect  $k$ -edge resonant inelastic x-ray scattering on magnetic excitations in a triangular-lattice antiferromagnet," *Phys. Rev. B* **92**, 035109 (2015).
  - [2] Rajiv R. P. Singh and David A. Huse, "Three-sublattice order in triangular- and kagomé-lattice spin-half antiferromagnets," *Phys. Rev. Lett.* **68**, 1766–1769 (1992).
  - [3] David A. Huse and Veit Elser, "Simple variational wave functions for two-dimensional heisenberg spin- $\frac{1}{2}$  antiferromagnets," *Phys. Rev. Lett.* **60**, 2531–2534 (1988).
  - [4] B. Bernu, P. Lecheminant, C. Lhuillier, and L. Pierre, "Exact

- spectra, spin susceptibilities, and order parameter of the quantum heisenberg antiferromagnet on the triangular lattice," *Phys. Rev. B* **50**, 10048–10062 (1994).
- [5] P. H. Y. Li, R. F. Bishop, and C. E. Campbell, "Quasiclassical magnetic order and its loss in a spin- $\frac{1}{2}$  heisenberg antiferromagnet on a triangular lattice with competing bonds," *Phys. Rev. B* **91**, 014426 (2015).
- [6] T. Ono, H. Tanaka, H. Aruga Katori, F. Ishikawa, H. Mitamura, and T. Goto, "Magnetization plateau in the frustrated quantum spin system  $\text{Cs}_2\text{CuBr}_4$ ," *Phys. Rev. B* **67**, 104431 (2003).
- [7] Hiroaki Kadowaki, Koji Ubukoshi, Kinshiro Hirakawa, Jos L.

- Martnez, and Gen Shirane, “Experimental study of new type phase transition in triangular lattice antiferromagnet  $\text{vcl}_2$ ,” *J. Phys. Soc. Jpn* **56**, 4027–4039 (1987).
- [8] R. Ishii, S. Tanaka, K. Onuma, Y. Nambu, M. Tokunaga, T. Sakakibara, N. Kawashima, Y. Maeno, C. Broholm, D. P. Gautreaux, J. Y. Chan, and S. Nakatsuji, “Successive phase transitions and phase diagrams for the quasi-two-dimensional easy-axis triangular antiferromagnet  $\text{rb 4 mn}(\text{moo 4})_3$ ,” *Eur. Phys. Lett.* **94**, 17001 (2011).
- [9] M. Poienar, F. Damay, C. Martin, J. Robert, and S. Petit, “Spin dynamics in the geometrically frustrated multiferroic  $\text{cucro}_2$ ,” *Phys. Rev. B* **81**, 104411 (2010).
- [10] S. Toth, B. Lake, S. A. J. Kimber, O. Pieper, M. Reehuis, A. T. M. N. Islam, O. Zaharko, C. Ritter, A. H. Hill, H. Ryll, K. Kiefer, D. N. Argyriou, and A. J. Williams, “ $120^\circ$  helical magnetic order in the distorted triangular antiferromagnet  $\alpha\text{-cacr}_2\text{O}_4$ ,” *Phys. Rev. B* **84**, 054452 (2011).
- [11] S. Toth, B. Lake, K. Hradil, T. Guidi, K. C. Rule, M. B. Stone, and A. T. M. N. Islam, “Magnetic soft modes in the distorted triangular antiferromagnet  $\alpha\text{-cacr}_2\text{O}_4$ ,” *Phys. Rev. Lett.* **109**, 127203 (2012).
- [12] Yutaka Shirata, Hidekazu Tanaka, Akira Matsuo, and Koichi Kindo, “Experimental realization of a spin-1/2 triangular-lattice heisenberg antiferromagnet,” *Phys. Rev. Lett.* **108**, 057205 (2012).
- [13] G. Koutoulakis, T. Zhou, Y. Kamiya, J. D. Thompson, H. D. Zhou, C. D. Batista, and S. E. Brown, “Quantum phase diagram of the  $s = \frac{1}{2}$  triangular-lattice antiferromagnet  $\text{ba}_3\text{cosb}_2\text{O}_9$ ,” *Phys. Rev. B* **91**, 024410 (2015).
- [14] Takuya Susuki, Nobuyuki Kurita, Takuya Tanaka, Hiroyuki Nojiri, Akira Matsuo, Koichi Kindo, and Hidekazu Tanaka, “Magnetization process and collective excitations in the  $s=1/2$  triangular-lattice heisenberg antiferromagnet  $\text{ba}_3\text{cosb}_2\text{O}_9$ ,” *Phys. Rev. Lett.* **110**, 267201 (2013).
- [15] Wing-Ho Ko and Patrick A. Lee, “Proposal for detecting spin-chirality terms in mott insulators via resonant inelastic x-ray scattering,” *Phys. Rev. B* **84**, 125102 (2011).
- [16] Ru Chen, Hyejin Ju, Hong-Chen Jiang, Oleg A. Starykh, and Leon Balents, “Ground states of spin- $\frac{1}{2}$  triangular antiferromagnets in a magnetic field,” *Phys. Rev. B* **87**, 165123 (2013).
- [17] Burkhard Schmidt and Peter Thalmeier, “Quantum fluctuations in anisotropic triangular lattices with ferromagnetic and antiferromagnetic exchange,” *Phys. Rev. B* **89**, 184402 (2014).
- [18] Philipp Hauke, Tommaso Roscilde, Valentin Murg, J Ignacio Cirac, and Roman Schmied, “Modified spin-wave theory with ordering vector optimization: spatially anisotropic triangular lattice and  $\text{j}_1\text{j}_2\text{j}_3$  model with heisenberg interactions,” *New Journal of Physics* **13**, 075017 (2011).
- [19] Masanori Kohno, Oleg A. Starykh, and Leon Balents, “Spinons and triplons in spatially anisotropic frustrated antiferromagnets,” *Nature Phys.* **3**, 790 (2007).
- [20] M. Swanson, J. T. Haraldsen, and R. S. Fishman, “Critical anisotropies of a geometrically frustrated triangular-lattice antiferromagnet,” *Phys. Rev. B* **79**, 184413 (2009).
- [21] Randy S. Fishman and Satoshi Okamoto, “Noncollinear magnetic phases of a triangular-lattice antiferromagnet and of doped  $\text{cuFeO}_2$ ,” *Phys. Rev. B* **81**, 020402 (2010).
- [22] E. A. Ghioldi, A. Mezio, L. O. Manuel, R. R. P. Singh, J. Oitmaa, and A. E. Trumper, “Magnons and excitation continuum in  $\text{xxz}$  triangular antiferromagnetic model: Application to  $\text{ba}_3\text{cosb}_2\text{O}_9$ ,” *Phys. Rev. B* **91**, 134423 (2015).
- [23] Nobuo Suzuki, Fumitaka Matsubara, Sumiyoshi Fujiki, and Takayuki Shirakura, “Absence of classical long-range order in an  $s = \frac{1}{2}$  heisenberg antiferromagnet on a triangular lattice,” *Phys. Rev. B* **90**, 184414 (2014).
- [24] Andreas Weichselbaum and Steven R. White, “Incommensurate correlations in the anisotropic triangular heisenberg lattice,” *Phys. Rev. B* **84**, 245130 (2011).
- [25] Philipp Hauke, “Quantum disorder in the spatially completely anisotropic triangular lattice,” *Phys. Rev. B* **87**, 014415 (2013).
- [26] Oleg A. Starykh, Wen Jin, and Andrey V. Chubukov, “Phases of a triangular-lattice antiferromagnet near saturation,” *Phys. Rev. Lett.* **113**, 087204 (2014).
- [27] John O. Fjærestad, Weihong Zheng, Rajiv R. P. Singh, Ross H. McKenzie, and Radu Coldea, “Excitation spectra and ground state properties of the layered spin- $\frac{1}{2}$  frustrated antiferromagnets  $\text{cs}_2\text{CuCl}_4$  and  $\text{cs}_2\text{CuBr}_4$ ,” *Phys. Rev. B* **75**, 174447 (2007).
- [28] Z. Z. Du, H. M. Liu, Y. L. Xie, Q. H. Wang, and J.-M. Liu, “Spin casimir effect in noncollinear quantum antiferromagnets: Torque equilibrium spin wave approach,” *Phys. Rev. B* **92**, 214409 (2015).
- [29] Z. Z. Du, H. M. Liu, Y. L. Xie, Q. H. Wang, and J.-M. Liu, “Magnetic excitations in quasi-one-dimensional helimagnets: Magnon decays and influence of interchain interactions,” *Phys. Rev. B* **94**, 134416 (2016).
- [30] Zheng Weihong, Ross H. McKenzie, and Rajiv R. P. Singh, “Phase diagram for a class of spin- $\frac{1}{2}$  heisenberg models interpolating between the square-lattice, the triangular-lattice, and the linear-chain limits,” *Phys. Rev. B* **59**, 14367–14375 (1999).
- [31] Weihong Zheng, John O. Fjærestad, Rajiv R. P. Singh, Ross H. McKenzie, and Radu Coldea, “Anomalous excitation spectra of frustrated quantum antiferromagnets,” *Phys. Rev. Lett.* **96**, 057201 (2006).
- [32] Weihong Zheng, John O. Fjærestad, Rajiv R. P. Singh, Ross H. McKenzie, and Radu Coldea, “Excitation spectra of the spin- $\frac{1}{2}$  triangular-lattice heisenberg antiferromagnet,” *Phys. Rev. B* **74**, 224420 (2006).
- [33] Richard P. Feynman, *Statistical Mechanics: A Set Of Lectures (Advanced Books Classics)*, 2nd ed., Advanced Books Classics (Westview Press, 1998).
- [34] S. M. Girvin, A. H. MacDonald, and P. M. Platzman, “Magneto-roton theory of collective excitations in the fractional quantum hall effect,” *Phys. Rev. B* **33**, 2481–2494 (1986).
- [35] Oleg A. Starykh, Andrey V. Chubukov, and Alexander G. Abanov, “Flat spin-wave dispersion in a triangular antiferromagnet,” *Phys. Rev. B* **74**, 180403 (2006).
- [36] Jason Alicea, Olexei I. Motrunich, and Matthew P. A. Fisher, “Theory of the algebraic vortex liquid in an anisotropic spin- $\frac{1}{2}$  triangular antiferromagnet,” *Phys. Rev. B* **73**, 174430 (2006).
- [37] Jason Alicea and Matthew P. A. Fisher, “Critical spin liquid at  $\frac{1}{3}$  magnetization in a spin- $\frac{1}{2}$  triangular antiferromagnet,” *Phys. Rev. B* **75**, 144411 (2007).
- [38] P. A. Maksimov, M. E. Zhitomirsky, and A. L. Chernyshev, “Field-induced decays in  $\text{xxz}$  triangular-lattice antiferromagnets,” *Phys. Rev. B* **94**, 140407 (2016).
- [39] Natalia Perkins and Wolfram Brenig, “Raman scattering in a heisenberg  $s = \frac{1}{2}$  antiferromagnet on the triangular lattice,” *Phys. Rev. B* **77**, 174412 (2008).
- [40] Natalia B. Perkins, Gia-Wei Chern, and Wolfram Brenig, “Raman scattering in a heisenberg  $s = \frac{1}{2}$  antiferromagnet on the anisotropic triangular lattice,” *Phys. Rev. B* **87**, 174423 (2013).
- [41] R. Coldea, D. A. Tennant, A. M. Tsvelik, and Z. Tylczynski, “Experimental realization of a 2d fractional quantum spin liquid,” *Phys. Rev. Lett.* **86**, 1335–1338 (2001).
- [42] Wei Chen and Oleg P. Sushkov, “Implications of resonant inelastic x-ray scattering data for theoretical models of cuprates,” *Phys. Rev. B* **88**, 184501 (2013).
- [43] Elaheh Ghorbani, Luca F. Tocchio, and Federico Becca, “Vari-

- ational wave functions for the  $s = \frac{1}{2}$  heisenberg model on the anisotropic triangular lattice: Spin liquids and spiral orders,” *Phys. Rev. B* **93**, 085111 (2016).
- [44] R. Coldea, D. A. Tennant, and Z. Tylczynski, “Extended scattering continua characteristic of spin fractionalization in the two-dimensional frustrated quantum magnet  $\text{Cs}_2\text{CuCl}_4$  observed by neutron scattering,” *Phys. Rev. B* **68**, 134424 (2003).
- [45] M. E. Zhitomirsky and A. L. Chernyshev, “Colloquium: Spontaneous magnon decays,” *Rev. Mod. Phys.* **85**, 219–242 (2013).
- [46] A. L. Chernyshev and M. E. Zhitomirsky, “Magnon decay in noncollinear quantum antiferromagnets,” *Phys. Rev. Lett.* **97**, 207202 (2006).
- [47] M. Mourigal, W. T. Fuhrman, A. L. Chernyshev, and M. E. Zhitomirsky, “Dynamical structure factor of the triangular-lattice antiferromagnet,” *Phys. Rev. B* **88**, 094407 (2013).
- [48] A. L. Chernyshev and M. E. Zhitomirsky, “Spin waves in a triangular lattice antiferromagnet: Decays, spectrum renormalization, and singularities,” *Phys. Rev. B* **79**, 144416 (2009).
- [49] S. A. Zvyagin, D. Kamenskyi, M. Ozerov, J. Wosnitza, M. Ikeda, T. Fujita, M. Hagiwara, A. I. Smirnov, T. A. Soldatov, A. Ya. Shapiro, J. Krzystek, R. Hu, H. Ryu, C. Petrovic, and M. E. Zhitomirsky, “Direct determination of exchange parameters in  $\text{Cs}_2\text{CuBr}_4$  and  $\text{Cs}_2\text{CuCl}_4$ : High-field electron-spin-resonance studies,” *Phys. Rev. Lett.* **112**, 077206 (2014).
- [50] J. van den Brink, “The theory of indirect resonant inelastic x-ray scattering on magnons,” *Europhys. Lett.* **80**, 47003 (2007).
- [51] Filomena Forte, Luuk J. P. Ament, and Jeroen van den Brink, “Magnetic excitations in  $\text{La}_2\text{CuO}_4$  probed by indirect resonant inelastic x-ray scattering,” *Phys. Rev. B* **77**, 134428 (2008).
- [52] R. W. Davies, S. R. Chinn, and H. J. Zeiger, “Spin-wave approach to two-magnon raman scattering in a simple antiferromagnet,” *Phys. Rev. B* **4**, 992–1004 (1971).
- [53] C. M. Canali and S. M. Girvin, “Theory of raman scattering in layered cuprate materials,” *Phys. Rev. B* **45**, 7127–7160 (1992).
- [54] J. Schlappa, T. Schmitt, F. Vernay, V. N. Strocov, V. Ilakovac, B. Thielemann, H. M. Rønnow, S. Vanishri, A. Piazzalunga, X. Wang, L. Braicovich, G. Ghiringhelli, C. Marin, J. Mesot, B. Delley, and L. Patthey, “Collective magnetic excitations in the spin ladder  $\text{Sr}_{14}\text{Cu}_{24}\text{O}_{41}$  measured using high-resolution resonant inelastic x-ray scattering,” *Phys. Rev. Lett.* **103**, 047401 (2009).
- [55] J. Schlappa, U. Kumar, K. J. Zhou, S. Singh, M. Mourigal, V. N. Strocov, A. Revcolevschi, L. Patthey, H. M. Rønnow, S. Johnston, and T. Schmitt, “Probing multi-spinon excitations outside of the two-spinon continuum in the antiferromagnetic spin chain cuprate  $\text{Sr}_2\text{CuO}_3$ ,” *Nature Communications* **9**, 5394 (2018).
- [56] Oleg A. Starykh, Andrey V. Chubukov, and Alexander G. Abanov, “Flat spin-wave dispersion in a triangular antiferromagnet,” *Phys. Rev. B* **74**, 180403 (2006).
- [57] Oleg A Starykh, “Unusual ordered phases of highly frustrated magnets: a review,” *Reports on Progress in Physics* **78**, 052502 (2015).
- [58] H. M. Rønnow, D. F. McMorrow, R. Coldea, A. Harrison, I. D. Youngson, T. G. Perring, G. Aeppli, O. Syljuåsen, K. Lefmann, and C. Rischel, “Spin dynamics of the 2d spin  $\frac{1}{2}$  quantum antiferromagnet copper deuteroformate tetradeuterate (cftd),” *Phys. Rev. Lett.* **87**, 037202 (2001).
- [59] Thomas P. Devereaux and Rudi Hackl, “Inelastic light scattering from correlated electrons,” *Rev. Mod. Phys.* **79**, 175–233 (2007).
- [60] F Vernay, T P Devereaux, and M J P Gingras, “Raman scattering for triangular lattices spin-1/2 heisenberg antiferromagnets,” *J. Phys.: Condens. Matter* **19**, 145243 (2007).